2-16-2021

# Cancer-associated exportin-6 upregulation inhibits the transcriptionally repressive and anticancer effects of nuclear profilin-1

Cuige Zhu

Sun-Joong Kim

Arshag Mooradian

Faliang Wang

Ziqian Li

*See next page for additional authors*

## Authors

Cuige Zhu, Sun-Joong Kim, Arshag Mooradian, Faliang Wang, Ziqian Li, Sean Holohan, Patrick L Collins, Keren Wang, Zhanfang Guo, Jeremy Hoog, Cynthia X Ma, Eugene M Oltz, Jason M Held, and Jieya Shao

Cell Reports

Article

# Cancer-associated exportin-6 upregulation inhibits the transcriptionally repressive and anticancer effects of nuclear profilin-1

## Graphical Abstract

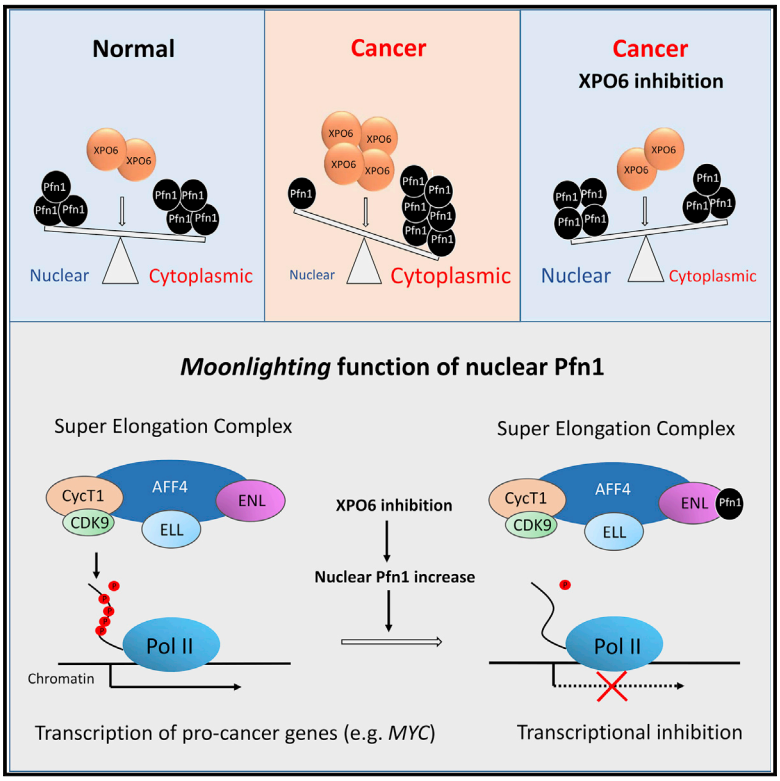


## Highlights

- The highly selective nuclear exporter exportin-6 is frequently upregulated in cancer
- Nuclear export of profilin-1 underlies the pro-cancer activity of exportin-6
- Nuclear profilin-1 inhibits super elongation complex and pro-cancer gene expression
- Exportin-6 loss sensitizes breast cancer cells to BET bromodomain inhibitor


## Authors

Cuige Zhu, Sun-Joong Kim, Arshag Mooradian, ..., Eugene M. Oltz, Jason M. Held, Jieya Shao

## Correspondence

shao.j@wustl.edu



## In Brief

By defining the moonlighting function of the small actin-binding protein profilin-1 in the nucleus as a transcriptional repressor and the prevalent upregulation of its nuclear exporter exportin-6 in diverse cancer types, Zhu et al. show that deregulation of protein subcellular localization is an important non-oncogene addiction with strong therapeutic potential.


Zhu et al., 2021, Cell Reports *34*, 108749
February 16, 2021 
https://doi.org/10.1016/j.celrep.2021.108749

CellPress

Cell Reports

CellPress
OPEN ACCESS

Article

# Cancer-associated exportin-6 upregulation inhibits the transcriptionally repressive and anticancer effects of nuclear profilin-1

Cuige Zhu,[1,8] Sun-Joong Kim,[1,8] Arshag Mooradian,[1] Faliang Wang,[1,2] Ziqian Li,[1,3] Sean Holohan,[1] Patrick L. Collins,[4,5] Keren Wang,[1] Zhanfang Guo,[1] Jeremy Hoog,[1] Cynthia X. Ma,[1,6] Eugene M. Oltz,[4,5] Jason M. Held,[1,6,7] and Jieya Shao[1,6,7,9,*]

[1]Department of Medicine, Washington University School of Medicine, St. Louis, MO 63110, USA
[2]Department of Surgical Oncology, The Children's Hospital, Zhejiang University School of Medicine, National Clinical Research Center for Child Health, Hangzhou 310052, China
[3]Department of Microbial and Biochemical Pharmacy, School of Pharmaceutical Sciences, Sun Yat-sen University, Guangzhou 510006, China
[4]Department of Pathology and Immunology, Washington University School of Medicine, St. Louis, MO 63110, USA
[5]Department of Microbial Infection and Immunity, The Ohio State University, Columbus, OH 43210, USA
[6]Siteman Cancer Center, Washington University School of Medicine, St. Louis, MO 63110, USA
[7]Department of Anesthesiology, Washington University School of Medicine, St. Louis, MO 63110, USA
[8]These authors contributed equally
[9]Lead contact
*Correspondence: shao.j@wustl.edu
https://doi.org/10.1016/j.celrep.2021.108749

## SUMMARY

Aberrant expression of nuclear transporters and deregulated subcellular localization of their cargo proteins are emerging as drivers and therapeutic targets of cancer. Here, we present evidence that the nuclear exporter exportin-6 and its cargo profilin-1 constitute a functionally important and frequently deregulated axis in cancer. Exportin-6 upregulation occurs in numerous cancer types and is associated with poor patient survival. Reducing exportin-6 level in breast cancer cells triggers antitumor effects by accumulating nuclear profilin-1. Mechanistically, nuclear profilin-1 interacts with eleven-nineteen-leukemia protein (ENL) within the super elongation complex (SEC) and inhibits the ability of the SEC to drive transcription of numerous pro-cancer genes including *MYC*. *XPO6* and *MYC* are positively correlated across diverse cancer types including breast cancer. Therapeutically, exportin-6 loss sensitizes breast cancer cells to the bromodomain and extra-terminal (BET) inhibitor JQ1. Thus, exportin-6 upregulation is a previously unrecognized cancer driver event by spatially inhibiting nuclear profilin-1 as a tumor suppressor.

## INTRODUCTION

In eukaryotic cells, the nuclear membrane compartmentalizes cellular contents into the cytoplasm and nucleus. For large macromolecules such as proteins and RNAs that exceed the diffusion limit of the nuclear pore complexes (NPCs), trafficking across the nuclear membrane is mediated by the importin and exportin proteins in the karyopherin β family (Güttler and Görlich, 2011). This evolutionarily conserved mechanism ensures the presence of the cargo molecules within their destined subcellular compartments at the levels appropriate for the specific cellular state. However, the physiological balance of many proteins across the nuclear membrane becomes dysregulated in cancer via different mechanisms, including altered expression of nucleocytoplasmic transporters (Hung and Link, 2011). For instance, tumor-suppressor proteins such as p53, FOXO2, p27, and pRb undergo nuclear exclusion and spatial inactivation in certain cancer cells due to upregulation of their nuclear exporter XPO1/CRM1, which shuttles hundreds of nuclear proteins containing leucine-rich nuclear export sequences (NESs) (Gravina et al., 2014; Hung and Link, 2011). XPO1 is a marker of poor cancer prognosis, and its inhibition showed anticancer benefits in various preclinical and clinical studies (Mahipal and Malafa, 2016). The XPO1-selective inhibitor Selinexor was recently approved to treat adult patients with relapsed or refractory multiple myeloma and diffuse large B cell lymphoma (DLBCL) (Gandhi et al., 2018; Kalakonda et al., 2020).

XPO6 is the most recently discovered member of the exportin family and is specific to the dimeric complex of nuclear actin and profilin (Pfn) (Stüven et al., 2003). Though capable of recognizing actin alone, the affinity and export activity of XPO6 toward the actin/Pfn complex are significantly higher (Stüven et al., 2003). Evolutionarily conserved from insects to mammals, XPO6 is essential for *Drosophila* embryonic development (Perrimon et al., 1989) yet transiently silenced in the amphibian *Xenopus* oocytes prior to meiotic maturation to increase the levels of

nuclear filamentous actin that physically stabilize their giant nuclei (Bohnsack et al., 2006). In addition, nuclear actin in its monomeric form regulates diverse processes including chromatin remodeling, RNA transcription, and DNA damage response (Virtanen and Vartiainen, 2017). The consensus from these studies is that nuclear actin positively regulates gene expression and cell proliferation (Virtanen and Vartiainen, 2017). Consistent with this, nuclear actin depletion occurs in growth-arrested normal breast epithelial cells but not their malignant counterparts, indicating a potentially pro-cancer effect of nuclear actin at least in the context of breast cancer (Spencer et al., 2011).

In contrast, the biological function of nuclear Pfn remains poorly understood, despite its presence in the nucleoplasm, nuclear speckles, and Cajal bodies (Skare et al., 2003). As the first actin-binding protein identified decades ago (Carlsson et al., 1977), the role of Pfn1, the ubiquitously expressed Pfn isoform, has been well demonstrated in cytoplasmic actin polymerization (Jockusch et al., 2007) and underlies its essentiality for many eukaryotic organisms (Balasubramanian et al., 1994; Verheyen and Cooley, 1994; Witke et al., 2001). Paradoxically, Pfn1 also shows tumor-inhibitory activities in breast, bladder, and pancreatic cancer models (Diamond et al., 2015; Wittenmayer et al., 2004; Yao et al., 2014; Zoidakis et al., 2012; Zou et al., 2007). Our prior study suggested that the anticancer activity of Pfn1 stems from its poorly understood nuclear functions that are spatially separate from its essential cytoplasmic functions (Diamond et al., 2015) and requires interaction with at least one nuclear protein containing the poly-L-proline (PLP) motif (XP $\geq$ 5; X = G, A, I, S, L) (Holt and Koffer, 2001). However, our current knowledge of PLP-containing binding partners of nuclear Pfn1 is limited to p42POP (Lederer et al., 2005) and SMN1 (Giesemann et al., 1999), neither of which has clear functional relevance to cancer.

As an essential protein rarely mutated, both the cancer relevance and underlying mechanism of Pfn1 remain unclear. Though largely unexplored in cancer, *XPO6* mRNA level is a poor prognostic marker for prostate cancer (Hao et al., 2016). XPO6 downregulation was detected in senescent human fibroblasts, positively linking it to proliferation (Park et al., 2011). Here, we report that XPO6 upregulation is a prevalent cancer-associated event that serves to indirectly reduce the anticancer function of Pfn1 in the nucleus as a transcriptional repressor while preserving its essential function in the cytoplasm.

## RESULTS

### XPO6 upregulation occurs in cancer and associates with poor patient survival

To investigate the cancer relevance of XPO6, we first examined The Cancer Genome Atlas (TCGA) datasets. *XPO6* mRNA is significantly upregulated in 19 cancer types compared to normal controls (~1.2–1.9-fold), with thyroid carcinoma being the only cancer type showing downregulation (Figure 1A; Table S1A). In breast cancer, the average upregulation of *XPO6* mRNA is ~1.5-fold. To increase the numbers of normal samples in our analysis, we used the combined RNA sequencing (RNA-seq) data from TCGA and The Genotype-Tissue Expression (GTEx) project (Wang et al., 2018). Statistically significant upregulation of *XPO6* mRNA levels was confirmed in all 16 cancer types for which processed data are available (Table S1B). Further analysis of matched tumor versus adjacent normal tissues in the TCGA dataset confirmed statistically significant *XPO6* mRNA upregulation in 13 cancer types (Table S1C). For breast cancer, 86.6% of the 112 cases with adjacent normal tissues overexpress *XPO6* by a median 1.36-fold (Figure 1B). The *XPO6* mRNA upregulation occurs independently of breast cancer subtype and stage (Figures S1A–S1C). We next examined the proteomic data of a cohort of 125 breast tumors and 18 normal breast tissue samples in the Clinical Proteomic Tumor Analysis Consortium (CPTAC) database. Unlike the other nuclear exportins (XPO1, 2, 4, 5, and 7), XPO6 peptides are detected in all tumor samples but none of the normal samples (Figure S1D), indicating their lower protein abundance in normal breast tissues below the detection limit.

We next examined a panel of breast cancer cell lines and two untransformed breast epithelial cell lines (HuMEC and MCF10A). Quantitative reverse transcriptase PCR (qRT-PCR) and western blot showed that both mRNA and protein levels of XPO6 are significantly higher in cancer versus normal cell lines. Similar to patient samples, XPO6 upregulation is independent of breast cancer subtype and occurs in both estrogen receptor (ER)-positive (MCF-7, T47D, CAMA-1) and ER-negative (MDA-MB-231, BT-549, HCC70) cells (Figures 1C and 1D).

We next examined the correlation between XPO6 and cancer patient survival. Using Kaplan-Meier (KM) Plotter (Nagy et al., 2018), we first performed pan-cancer Kaplan-Meier analysis between *XPO6* mRNA levels and overall survival (OS) using the TCGA RNA-seq data. We observed a statistically significant association between high *XPO6* mRNA levels and worse OS for bladder, kidney renal clear cell, and liver hepatocellular carcinomas (Figure 1E). For breast cancer, the correlation followed a similar trend, with the median OS of the low XPO6 group nearly doubling the high XPO6 group despite being statistically insignificant ($p = 0.22$) (Figure 1E). However, statistical significance ($p = 0.031$) was reached among stage II patients (~60% of the dataset) (Figure 1F) but not patients at other stages (Figure S2A). Though not statistically significant, the association between *XPO6* mRNA levels and OS was preferentially detected in lymph-node-positive patients with no clear dependence on ER status (Figures S2B and S2C). No association between *XPO6* mRNA and progression-free survival (PFS) was observed, regardless of lymph node status (Figure S2D).

Next, we analyzed breast cancer microarray data using the Gene Expression Omnibus (GEO) and European Genome-phenome Archive (EGA) datasets available at KM Plotter. In the combined datasets, we observed nearly significant correlation ($p = 0.066$) between high *XPO6* mRNA levels and worse relapse-free survival (RFS) in lymph-node-positive, but not lymph-node-negative, patients (Figure S2E), and this was confirmed using an individual dataset (GSE21653) (Finetti et al., 2008) (Figure S2F). Statistically significant correlations between *XPO6* mRNA and RFS were detected for both ER-negative (GSE21653) and ER-positive (GSE9195) patients in a dataset-dependent fashion (Finetti et al., 2008; Loi et al., 2008) (Figures S2G and S2H). In addition, we observed statistically significant

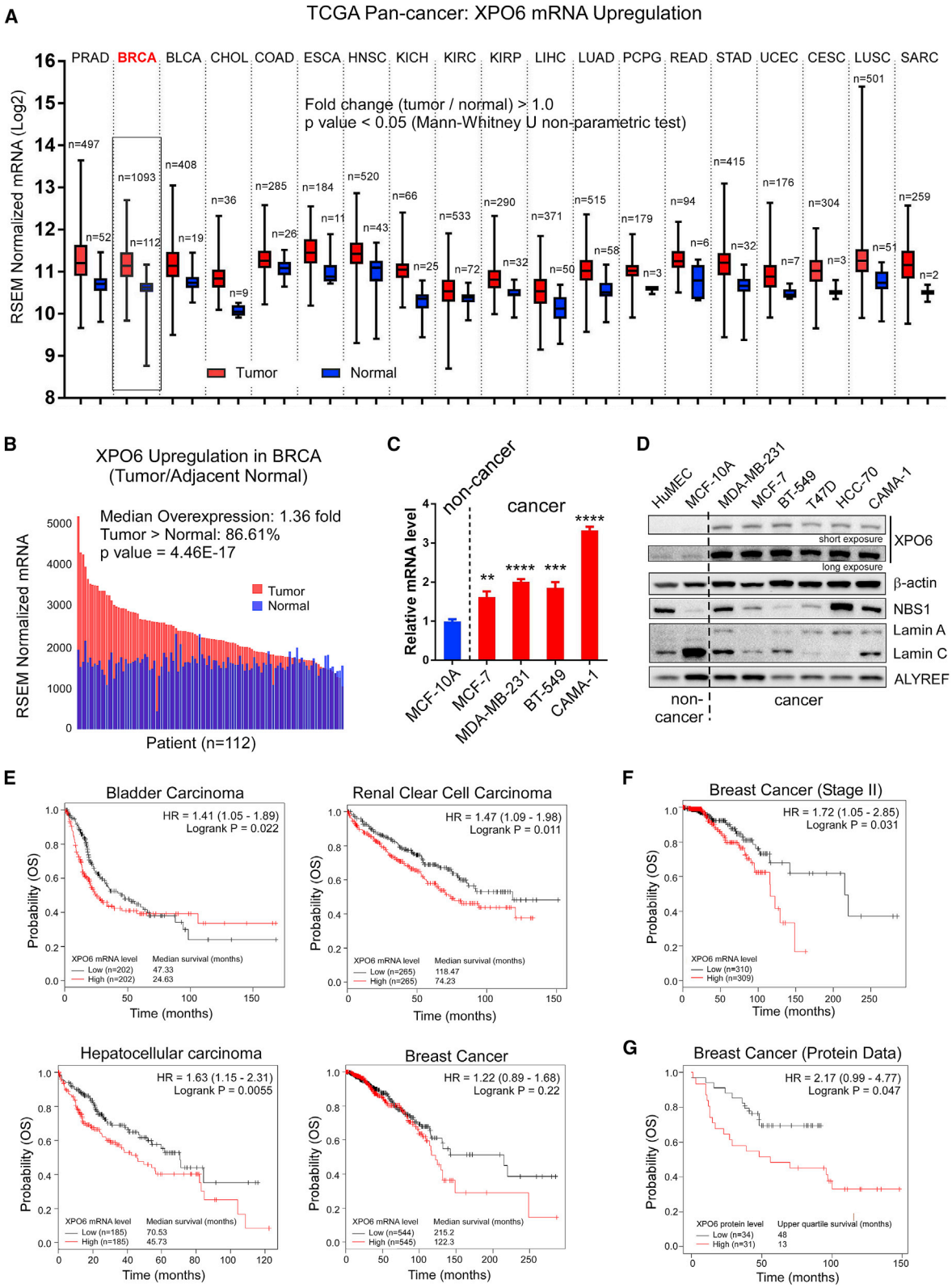


*(legend on next page)*

association between high XPO6 protein levels and worse OS of a cohort of 65 breast cancer patients (Tang et al., 2018) (Figure 1G), the only proteomic dataset available at KM Plotter for outcome analysis. Taken together, our findings demonstrate that XPO6 upregulation occurs in a large number of tumor types including breast cancer, and this is associated with poor patient survival.

## XPO6 is required for cancer cell growth

Hypothesizing that cancer cells may be addicted to XPO6, we silenced it in three breast cancer cell lines expressing high levels of XPO6 (MCF-7, T47D, MDA-MB-231; Figures 1C and 1D) and the non-cancer MCF10A cells. Two XPO6 short hairpin RNAs (shRNAs) significantly inhibited the growth of all three cancer cell lines (Figures 2A–2C). XPO6 knockdown also inhibited the growth of human soft tissue sarcoma SK-UT-1 and SK-LM-1 cell lines (Figures S3A and S3B). Interestingly, it showed no growth effect on MCF10A cells, suggesting that normal epithelial cells without XPO6 upregulation may be more tolerant of its loss. Conversely, overexpressing XPO6 in MCF10A cells increased their growth (Figure 2D), supporting the positive impact of XPO6 on cell growth.

To confirm that the growth phenotype of XPO6 knockdown was due to on-target effects, we stably expressed wild-type (WT) and RNA-inhibitor-resistant (RNAi-Res) XPO6 in MCF-7 cells (Figure S3C). While shXPO6 #3 inhibited the growth of XPO6(WT) MCF-7 cells, this effect was significantly rescued by XPO6(RNAi-Res) (Figure 2E). Multiple G1/S transition markers were downregulated by XPO6 knockdown in the XPO6(WT) cells, including p-Rb(Ser$^{795}$), E2F1, and cyclin D1, which were rescued by XPO6(RNAi-Res) (Figure 2E). Bromodeoxyuridine (BrdU) labeling of MCF-7 cells was reduced by XPO6 knockdown (Figure 2F). DNA content analysis of synchronized MCF-7 cells further confirmed the inhibitory effect of XPO6 knockdown on S-phase entry (Figure 2G).

Next, we implanted shLUC- and shXPO6-#3-infected MCF-7 cells expressing XPO6(WT) or XPO6(RNAi-Res) into the mammary fat pads of female nude mice supplemented with estrogen pellets. XPO6 knockdown in the XPO6(WT) cells significantly reduced tumor growth rate (Figure 3A), which was confirmed by endpoint tumor weights (Figure 3B). This effect was markedly attenuated in the XPO6(RNAi-Res) cells, and the difference in tumor volumes and weights between shXPO6 #3 and shLUC groups was non-significant (Figures 3A and 3B). Despite the incomplete rescue, presumably due to off-target effects of shXPO6 #3, our data sufficiently demonstrate the tumor-inhibitory effect of XPO6 loss. Staining the tumors for Ki67 and p-Rb(Ser$^{795}$) revealed that XPO6 knockdown in XPO6(WT) but not XPO6(RNAi-Res) cells reduced proliferation (Figures 3C and 3D), confirming the *in vitro* findings.

For further validation, we used CRISPR/Cas9 to knock out *XPO6* in MDA-MB-231 cells. We chose Cas9(D10A) nickase (Cas9n) to increase editing specificity and designed four pairs of single guide RNAs (sgRNAs) targeting *XPO6*. All four pairs reduced XPO6 protein level (Figure S4A). Compared to controls, *XPO6* knockout (KO) MDA-MB-231 cells grew significantly slower, phenocopying XPO6 knockdown in MCF-7 cells (Figure S4A). Single clones showed even stronger effects (Figures S4B and S4C). BrdU labeling and DNA content analysis displayed evidence of G1/S arrest and cell-cycle inhibition, similar to XPO6 knockdown effects in MCF-7 cells (Figures S4D and S4E). Thus, our data suggest a strong reliance of breast cancer cells on XPO6 function, which manifests at least partially through an effect on cell-cycle progression.

## Nuclear Pfn1 is required for the growth-inhibitory effect of XPO6 loss

XPO6 is a specific nuclear exporter for the Pfn/actin complex (Stüven et al., 2003). XPO6 knockdown and KO caused significant nuclear accumulation of endogenous Pfn1 (Figures 4A and S5A). Nuclear accumulation of exogenous yellow fluorescent protein (YFP)-tagged Pfn1 was similarly induced by XPO6 loss (Figures S5B–S5D). Pfn1 is a poorly understood tumor suppressor that is paradoxically essential for eukaryotic cells. Restricting Pfn1 expression to the nucleus versus cytoplasm in our prior study indicated that the tumor-suppressive activity of Pfn1 stems at least in part from its nuclear functions, spatially separate from its essential role in the cytoplasm (Diamond et al., 2015). To test whether the anticancer effect of XPO6 loss is caused by nuclear Pfn1 buildup, we asked whether this effect can be abolished by removing cellular Pfn1. Thus, we performed single or double knockdown of Pfn1 and XPO6 in the MCF-7 cells (Figure 4B). Consistent with the prior report that XPO6 can export nuclear actin independently of Pfn1 (Stüven et al., 2003), nuclear YFP-actin accumulated upon XPO6 knockdown in Pfn1-silenced cells (Figure S5E). However, unlike in the control cells, XPO6 knockdown in the Pfn1-silenced MCF-7 cells caused no growth inhibition (Figures 4B and S5F), suggesting that nuclear Pfn1 buildup underlies the anticancer effect of XPO6 loss.

To confirm this finding, we next exploited the *Pfn1*-null chondrocytes derived from the cartilage-specific *Pfn1* KO mice (Böttcher et al., 2009). Though displaying various abnormalities,

**Figure 1. XPO6 upregulation occurs in cancer and associates with poor patient survival**

(A) Pan-cancer *XPO6* mRNA levels in the TCGA cohorts. Whiskers represent min-max. Mann-Whitney U non-parametric test was used to compare between normal and tumor samples for each cancer type. RSEM, RNA-seq by expectation maximization.

(B) *XPO6* mRNA levels of 112 breast tumors in the TCGA dataset with adjacent normal tissues. p value was based on Wilcoxon Signed Rank non-parametric test.

(C) qRT-PCR of *XPO6* mRNA levels in breast epithelial cell lines. One-way ANOVA and Dunnett's multiple comparisons tests were used to compare between MCF-10A and breast cancer cell lines. Data are mean ± SEM. **p < 0.01; ***p < 0.001; ****p < 0.0001.

(D) Western blot of XPO6 in untransformed and transformed breast epithelial cell lines, with different cytoplasmic and nuclear proteins as controls.

(E) Univariate Kaplan-Meier analysis of the association between *XPO6* mRNA levels and the overall survival (OS) of TCGA patients with bladder, renal clear cell, hepatocellular, and breast carcinomas.

(F) Univariate Kaplan-Meier analysis of the association between *XPO6* mRNA levels and the OS of stage II breast cancer patients within the TCGA cohort.

(G) Univariate Kaplan-Meier analysis of the association between XPO6 protein levels and the OS of a cohort of 65 breast cancer patients.

p values for (E)–(G) were based on log-rank tests. See also Figures S1 and S2 and Tables S1A–S1C.

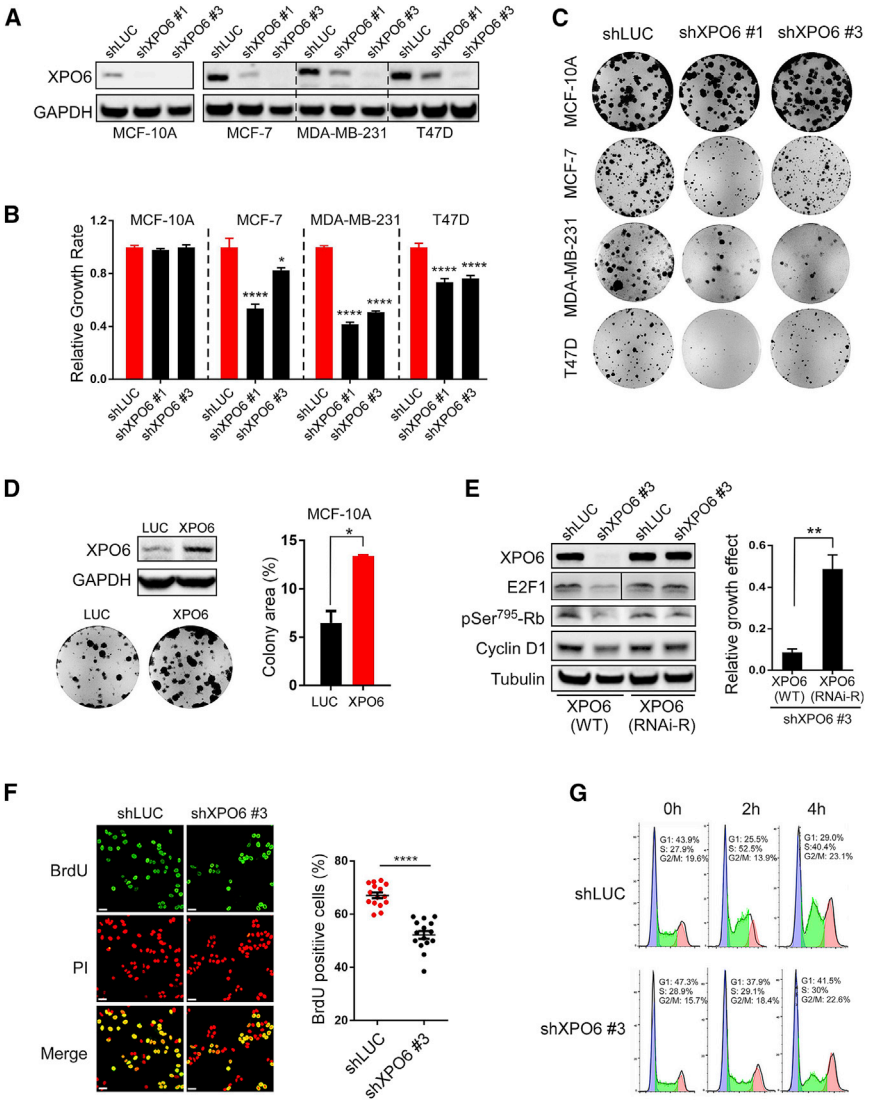


**Figure 2. XPO6 is required for breast cancer cell growth *in vitro***

(A) Human breast epithelial cell lines were infected with a small hairpin targeting luciferase (shLUC) and two different XPO6 shRNAs.

(B) Relative growth effects of XPO6 knockdown by dividing normalized Alamar blue values (day 9/1) of shXPO6 versus shLUC cells. Data are mean ± SEM of a representative experiment (sextuples per condition). p values were based on one-way ANOVA and Dunnett's multiple comparison tests.

(C) Colony formation assay using cells in (A).

(D) Colony formation assay using MCF-10A cells infected with XPO6 or luciferase. Colony areas were expressed as percentages. Data are mean ± SEM of a representative experiment (triplicates per condition).

(E) MCF-7 cells expressing WT or RNAi-Res XPO6 were infected with shLUC or shXPO6 #3 and subjected to Western blot analysis. Lanes for the E2F1 blot were cropped and rearranged from the same blot (indicated by the black line). Relative growth effects of XPO6 knockdown were calculated by normalizing colony areas of shXPO6 versus shLUC cells. Data are mean ± SD of one representative experiment (triplicates per condition).

(F) MCF-7 cells infected with shLUC or shXPO6 #3 were labeled with BrdU and stained for BrdU or with propidium iodide (PI). Fifteen random fields were quantified. Percent BrdU positivity of cells in all images is shown. Data are mean ± SEM. Scale bars, 40 μm.

(G) MCF-7 cells from (F) were synchronized by double thymidine block, released for different hours, and analyzed for DNA contents.

p values for (D)–(F) were based on unpaired t test. *p < 0.05; **p < 0.01; ***p < 0.001; ****p < 0.0001. All results were confirmed by three independent experiments. See also Figures S3 and S4.

these cells are viable in part due to the compensation from Pfn2 (Böttcher et al., 2009). We previously showed that the morphological and growth defects of *Pfn1* null chondrocytes can be rescued by Pfn1 that is untagged or fused to a NES but not a nuclear localization sequence (NLS) (Diamond et al., 2015). XPO6 knockdown caused no growth inhibition of *Pfn1*-null chondrocytes infected with an empty vector or YFP (Figures 4C and 4D). Re-expressing untagged or YFP-tagged Pfn1 restored growth inhibition by XPO6 knockdown (Figures 4C, 4D, S5G, and S5H). However, YFP-Pfn1 tagged with an NES, which converts it to a cargo of XPO1 and prevents its nuclear buildup by XPO6 loss, could not restore the shXPO6-induced growth inhibition (Figures 4D and S5H). Together, these data suggest that nuclear Pfn1 accumulation is the underlying cause for cell growth inhibition by XPO6 loss. Notably, the growth inhibition caused by XPO6 knockdown in the mouse chondrocytes differs from its lack of effect in the human mammary epithelial MCF-10A cells. This suggests that non-cancer cells, depending on tissue origin and cellular contexts, may have different sensitivity to nuclear Pfn1 accumulation.

Unlike the near-uniform XPO6 upregulation in cancer, Pfn1 shows mixed patterns of dysregulation. Out of the 12 TCGA cancer types in which *Pfn1* mRNA is significantly altered, seven show upregulation and five show downregulation (Figure S6A; Table S1D). In TCGA breast tumors, *Pfn1* mRNA is significantly upregulated (Figures S6A and S6B), and its protein level is markedly higher in the same panel of breast cancer cell lines overexpressing XPO6 (Figure S6C). However, in the CPTAC dataset, Pfn1 protein is significantly downregulated in the breast tumors (Figure S6D). Mixed associations between Pfn1 levels and breast cancer survival were also observed. While high *Pfn1* mRNA levels correlate with better survival of stage II (Figure S6E) and lymph-node-negative (Figure S6F; p = 0.12, statistically insignificant) TCGA patients, an opposite trend was observed in the combined GEO and EGA datasets where high *Pfn1* mRNA levels correlate with worse survival of lymph-node-negative patients (Figure S6G). Further testing of an individual GEO dataset (GSE21653, showing negative correlation

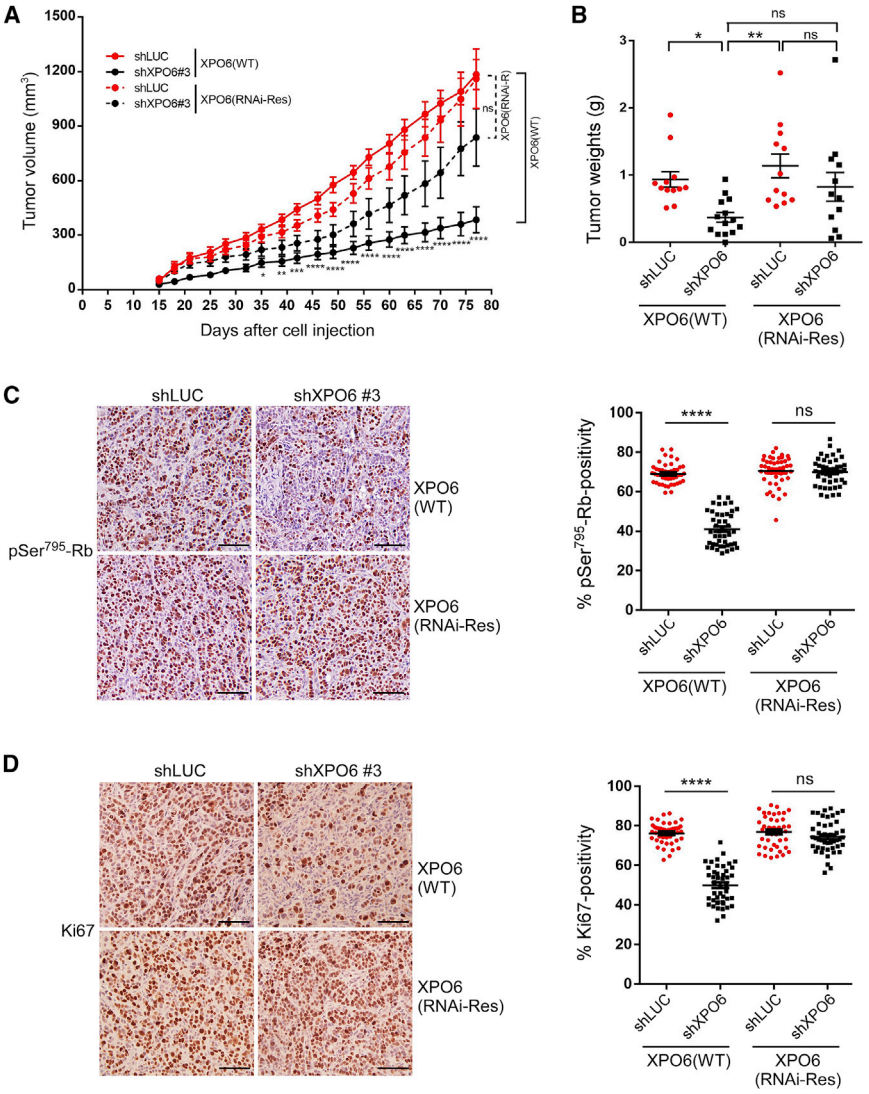


**Figure 3. XPO6 loss inhibits breast cancer growth *in vivo***

(A) MCF-7 cells expressing XPO6(WT) or XPO6(RNAi-Res) were infected with shLUC or shXPO6 #3 and inoculated in female nude mice (n = 6). Caliper measurement of tumors began at day 15. Two-way ANOVA and Sidak's multiple comparison tests were used to compare tumor volumes between shLUC and shXPO6 groups.

(B) Endpoint tumor weights. p values were based on one-way ANOVA and Tukey's multiple comparison tests.

(C and D) Three randomly selected tumors per group were immunostained for p-Rb(Ser$^{795}$) (C) and Ki67 (D). Positive tumor cells from random fields of each image were normalized against total tumor cells stained by hematoxylin. Each dot represents 300–450 tumor cells. Scale bars, 100 μm.

p values were based on one-way ANOVA and Tukey's multiple comparison tests. All data are mean ± SEM. *p < 0.05; **p < 0.01; ***p < 0.001; ****p < 0.0001.

between XPO6 and survival of lymph-node-positive patients in Figure S2F) revealed positive versus negative associations between *Pfn1* mRNA levels and the survival of lymph-node-negative and lymph-node-positive patients, respectively (Figure S6H). Nevertheless, no association between Pfn1 protein levels and survival was observed in the same proteomic dataset (Figure S6I) that showed significant association between high XPO6 and worse survival (Figure 1G). These variable results regarding Pfn1 expression and outcome associations, in clear contrast to XPO6, are consistent with the pleiotropic functions of Pfn1 and suggest that its tumor-supportive versus inhibitory activities are balanced in cancer cells stochastically. Therefore, total Pfn1 levels do not accurately reflect its anti-cancer activities.

## Nuclear Pfn1 interacts with the SEC

In addition to nuclear entry, our prior study suggested that Pfn1's ability to bind PLP motifs is also important for its anti-cancer activity (Diamond et al., 2015). Although PLPs mediate the direct interaction of Pfn1 with a multitude of cytoplasmic proteins, few nuclear-binding partners of Pfn1 are known. Thus, we performed immunoprecipitation (IP) of NLS-tagged YFP-Pfn1 from MDA-MB-231 nuclear extracts followed by mass spectrometry (MS) analysis to identify associated proteins. We used YFP as a non-specific binding control and a mutant NLS-Pfn1(S137D) unable to bind PLPs (Diamond et al., 2015) to exclude PLP-independent interactions (Figure 5A). Based on a 1% peptide false discovery rate and a relative protein expression ratio of >1.5 in the NLS-Pfn1(WT) versus YFP and NLS-Pfn1 S137D, we identified 37 proteins interacting with NLS-Pfn1(WT) in a PLP-dependent fashion (Table S2).

Three proteins contain the canonical Pfn1-interacting PLP motifs. They are BOD1L1, SFPQ, and MLLT1/ENL. BOD1L1 is a limitedly characterized protein with a role in DNA replication fork stability (Higgs et al., 2015). SFPQ is a multi-functional protein involved in pre-mRNA splicing and context-dependent transcriptional regulation (Fox and Lamond, 2010). ENL is an acetyllysine-binding transcriptional activator functioning primarily within the multi-component SEC. The SEC is a positive regulator of transcriptional elongation by phosphorylating Ser$^2$ of the Rpb1 subunit of RNA polymerase II (RNA Pol II) via the associated p-TEFb dimeric complex comprising Cdk9 and cyclin T1 or T2. This releases RNA Pol II from the "paused" state at the promoter proximal regions of many active genes and leads to their productive elongation (Luo et al., 2012b). Notably, in addition to ENL, we detected three SEC components by MS including AFF4, ELL,

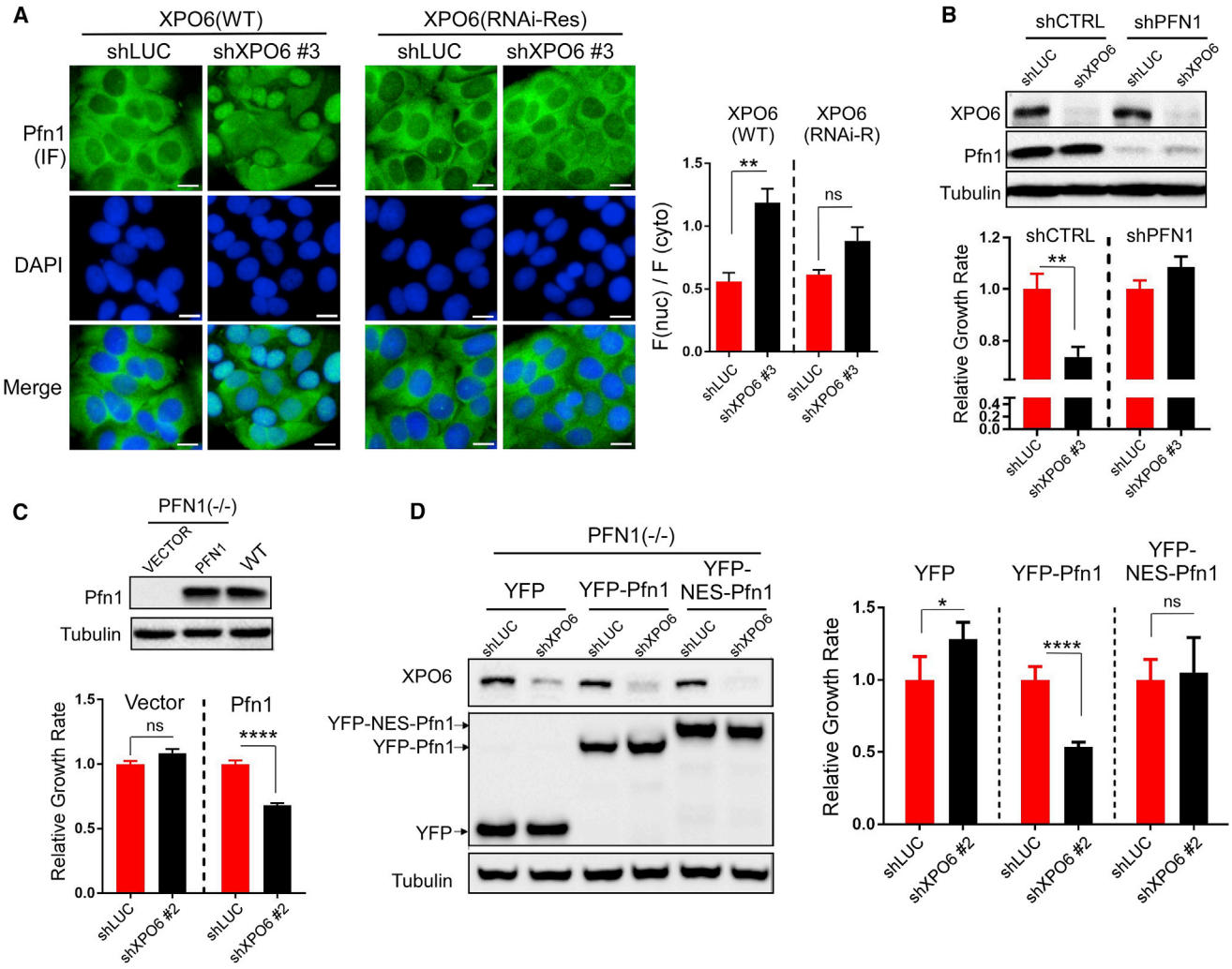


**Figure 4. Nuclear Pfn1 is required for the growth inhibitory effect of XPO6 loss**

(A) MCF-7 cells expressing XPO6(WT) or XPO6(RNAi-Res) were infected with shLUC or shXPO6 #3 and subjected to immunofluorescence staining for endogenous Pfn1 and nuclear staining by DAPI. Representative images and quantitative analysis of nuclear versus cytoplasmic fluorescence intensity are shown. Over 500 cells per condition were analyzed. Data are mean ± SEM. p values were based on unpaired t tests. Scale bars, 20 μm.

(B) MCF-7 cells were infected individually or simultaneously with shPFN1 (#2) (controlled by shCTRL) and shXPO6 #3 (controlled by shLUC). Relative cell growth rates were expressed as day 11/day 1 ratios as described in Figure 2B.

(C and D) *Pfn1*-null mouse chondrocytes were first infected with untagged Pfn1 (controlled by empty vector; C) or YFP-Pfn1 with or without an NES tag (controlled by YFP; D), followed by further infection with shLUC or shXPO6 #2 (recognizing mouse XPO6). Cells were subjected to western blot (Pfn1 antibody [C] and GFP antibody [D]) and growth analyses as described in (B).

For (B)–(D), relative growth of shLUC cells in each subgroup was arbitrarily set to 1. Data are mean ± SEM of a representative experiment (sextuplicates per condition). p values were based on unpaired t tests. **$p < 0.01$; ****$p < 0.0001$. Results were confirmed by three independent experiments. See also Figures S5 and S6 and Table S1D.

and cyclin T1, all of which preferentially bound NLS-Pfn1(WT) over NLS-Pfn1(S137D) and YFP (Figure 5B).

Focusing on SEC, we confirmed the MS data by co-IP and western blot using MCF-7 cells. In addition to ENL and Cyclin T1, we detected interactions of Cdk9 and Rbp1 with NLS-Pfn1(WT) but not NLS-Pfn1(S137D) or YFP (Figure 5C). We could not validate AFF4 interaction due to the performance issue of the antibody. To confirm the interaction of the SEC with endogenous Pfn1, we performed reciprocal IPs of ENL and cyclin T1. We detected specific co-precipitation of endogenous Pfn1 by ENL antibody and, to a much lesser extent, cyclin T1 antibody (Figure 5D). While similar amounts of Cdk9 were co-precipitated by ENL and cyclin T1, less ENL was pulled down indirectly by cyclin T1 than directly by ENL antibody. This is consistent with the fact that p-TEFb (cyclin T1/Cdk9) associates with different partners besides SEC (e.g., BET domain proteins) (Luo et al., 2012a), and further implicates that the Pfn1/SEC interaction is mediated directly by the PLP motif in ENL. Consistent with this, cyclin T1/Pfn1 interaction was significantly reduced by ENL knockdown (Figure 5E). In addition, we performed size-

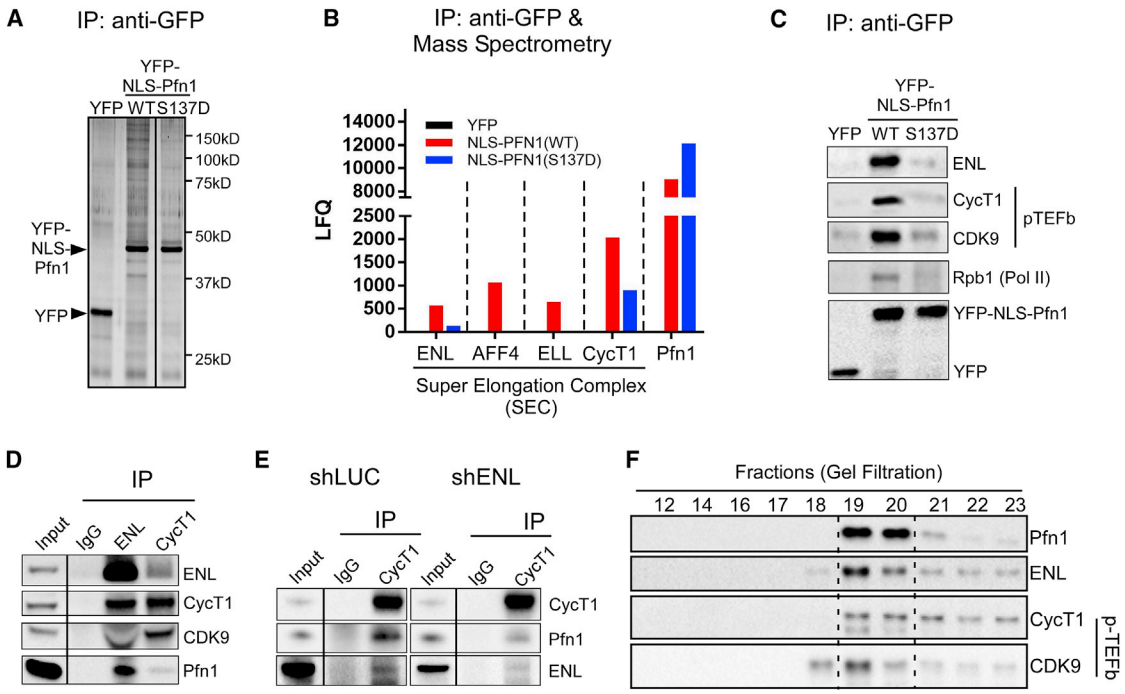


**Figure 5. Nuclear Pfn1 interacts with the SEC**

(A) IP of YFP or YFP-NLS-Pfn1(WT or S137D) from nuclear extracts of MDA-MB-231 stable cells by a GFP antibody, followed by silver staining.

(B) Eluates from (A) were analyzed by liquid chromatography-MS. Proteins specifically bound to NLS-Pfn1(WT) were identified using label-free quantification (LFQ) intensity and a threshold of >1.5-fold-higher intensity over those bound to YFP and NLS-Pfn1(S137D). LFQ intensities of detectable SEC components are shown.

(C) Confirmation of the interaction between NLS-Pfn1(WT) and SEC by anti-GFP co-IP as in (B) using nuclear extracts of stable MCF-7 cells, followed by western blot.

(D) Interaction between the SEC and endogenous Pfn1 in MCF-7 cells. ENL and cyclin T1 were pulled down followed by western blot.

(E) Cyclin T1 pulldown from shLUC- versus shENL-infected MCF-7 cells, followed by western blot for endogenous Pfn1 and other proteins. In total, 50-fold-less input was used for the Pfn1 blot given the small fraction of nuclear Pfn1 (most in the cytoplasm) interacting with the SEC.

(F) Size-exclusion chromatography and western blot analyses of nuclear extracts of MDA-MB-231 cells for endogenous Pfn1 and SEC components.

Results in (C)–(F) were confirmed by three independent experiments. Lanes in (A), (D), and (E) were cropped and rearranged from the same blots for clarity of presentation (indicated by the black lines). See also Table S2.

exclusion chromatography using MDA-MB-231 nuclear extracts. We detected partially overlapping distribution of p-TEFb and ENL, consistent with a prior report (Luo et al., 2012a). Importantly, endogenous Pfn1 showed a narrow size distribution that overlaps with both ENL and p-TEFb (Figure 5F). Collectively, our data revealed a previously unknown interaction between nuclear Pfn1 and the SEC via the direct binding of Pfn1 to the PLP motif within ENL.

## Nuclear Pfn1 inhibits SEC-dependent transcription of c-MYC

The role of the SEC in transcriptional checkpoint regulation is well known for developmental and stimulus-induced genes. In the context of cancer, the best-characterized SEC target gene is *MYC* (Luo et al., 2012b). To determine if the interaction of nuclear Pfn1 with the SEC is functionally relevant to its anticancer activity, we examined the effect of NLS- or NES-tagged YFP-Pfn1 on *MYC* expression by qRT-PCR (Figures 6A, 6B, S7A, and S7B). NLS-Pfn1(WT), but not NES-Pfn1(WT), significantly decreased *MYC* mRNA levels in both breast cancer cell lines and untransformed MCF-10A cells. The PLP-binding defective NLS-Pfn1(S137D) did not inhibit *MYC* expression, instead slightly increasing its levels (Figures 6B and S7B). Similarly, *MYC* mRNA levels were decreased by XPO6 knockdown, and the effect was rescuable by XPO6(RNAi-Res) (Figures 6C and S7C). Analyzing tumors from the MCF-7 xenograft experiment (Figure 3) showed that *MYC* mRNA downregulation by XPO6 knockdown also occurred *in vivo* (Figure 6D).

To causally link Pfn1 to *MYC* reduction by XPO6 knockdown, we used the *Pfn1*-null mouse chondrocytes described in Figures 4C and 4D (Böttcher et al., 2009). Consistent with nuclear Pfn1 mediating the effect of XPO6 knockdown, we observed no inhibition of *MYC* expression by XPO6 knockdown in the absence of Pfn1. However, *MYC* was inhibited when Pfn1 was re-expressed (Figure 6E). Conversely, Pfn1 knockdown significantly increased *MYC* mRNA levels (Figure 6F).

We next sought for clinical evidence in the TCGA datasets for transcriptional inhibition of *MYC* by nuclear Pfn1. We found a positive correlation between *MYC* and *XPO6* mRNA levels (Spearman correlation coefficient $\rho > 0$) in 25 out of 32 cancer types, with 15 (including breast cancer) being statistically significant (Figure 6G; Table S3). Among the 15 cancer types, $\rho$ values

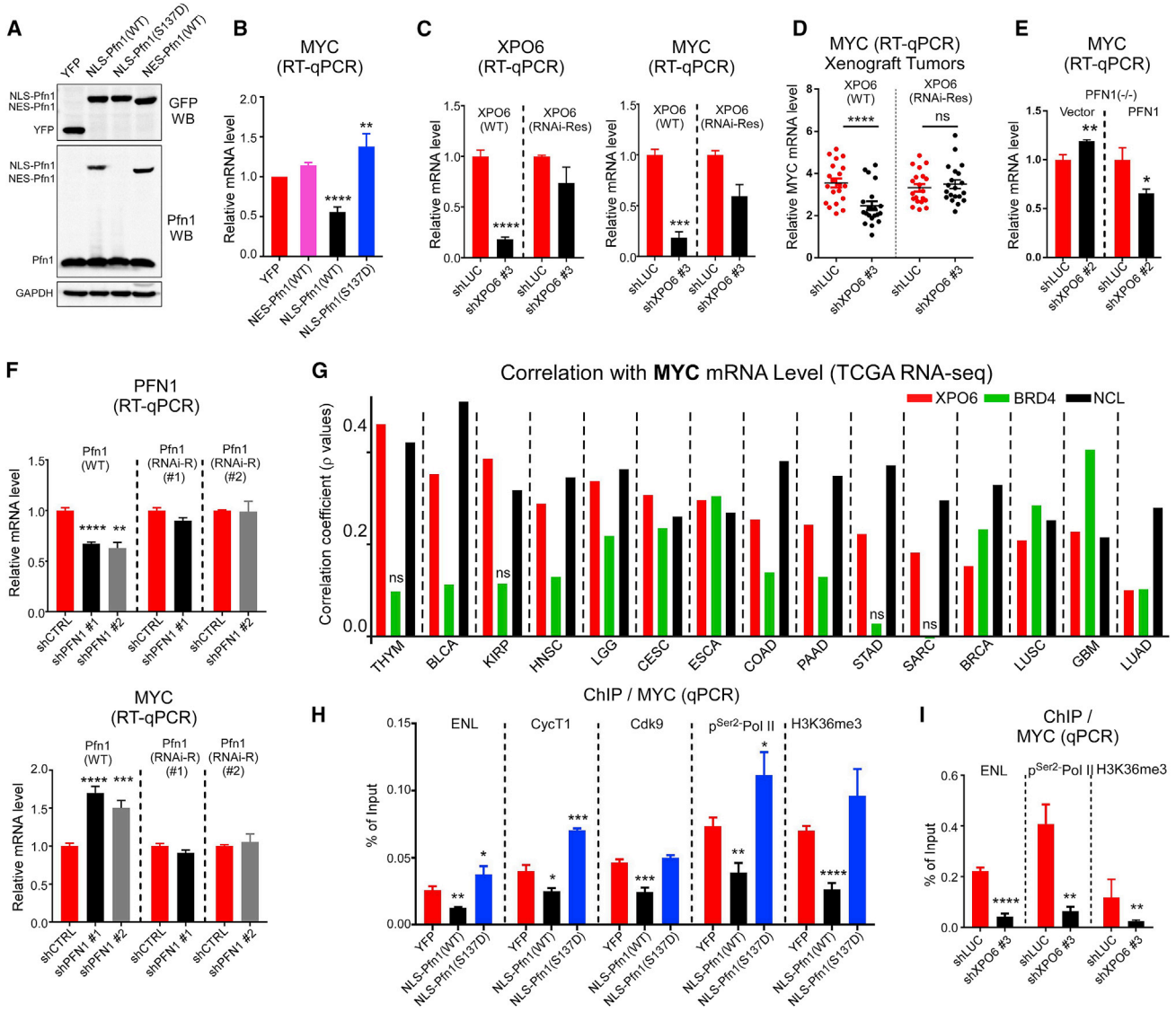


**Figure 6. Nuclear Pfn1 inhibits SEC function**

(A) Western blot of NLS- or NES-tagged YFP-Pfn1 relative to endogenous Pfn1 by GFP or Pfn1 antibodies. S137D, residing in the epitope of the Pfn1 antibody, abolishes the detection.

(B) qRT-PCR of *MYC* in MCF-7 cells in (A). p values were based on unpaired t test relative to YFP control.

(C) qRT-PCR of *XPO6* and *MYC* in MCF-7 cells expressing XPO6(WT) or XPO6(RNAi-Res) and infected with shLUC or shXPO6 (#3). p values were based on unpaired t test by comparing shLUC versus shXPO6 #3.

(D) qRT-PCR of *MYC* in XPO6 KD/rescue MCF-7 xenograft samples (10 tumors/group, 2 technical replicates/tumor) from Figure 3. p values were based on unpaired t test.

(E) qRT-PCR of *MYC* in *Pfn1*-null chondrocytes infected first with vector or Pfn1 and subsequently with shLUC or shXPO6 #2 (recognizing mouse XPO6). p values were based on unpaired t test.

(F) qRT-PCR of *MYC* and *Pfn1* in MCF-7 cells expressing Pfn1(WT) or Pfn1(RNAi-Res) and infected with scrambled shCTRL or shPFN1 #1 or #2. p values were based on unpaired t test by comparing shCTRL versus shPFN1.

(G) Correlations of *MYC* mRNA levels with *XPO6*, *BRD4*, and *NCL* in different TCGA datasets. The y axis represents Spearman's correlation coefficients (ρ). Fifteen cancer types in which statistically significant positive correlations between *XPO6* and *MYC* expression are shown (ρ > 0; FDR q values < 0.05).

(H) ChIP using antibodies for ENL, cyclin T1, Cdk9, p-Rpb1(Ser$^2$), and H3K36me3 from MCF-7 cells expressing YFP or YFP-NLS-Pfn1(WT or S137D) followed by *MYC* qPCR. p values were based on unpaired t test.

(I) ChIP using antibodies for ENL, p-Rpb1(Ser$^2$), and H3K36me3 from MCF-7 cells infected with shLUC or shXPO6 #3 followed by *MYC* qPCR.

p values were based on unpaired t test. All data (except A and G) represent mean ± SEM of representative experiments, which were confirmed at least three times. *p < 0.05; **p < 0.01; ***p < 0.001; ****p < 0.0001. See also Figure S7 and Table S3.

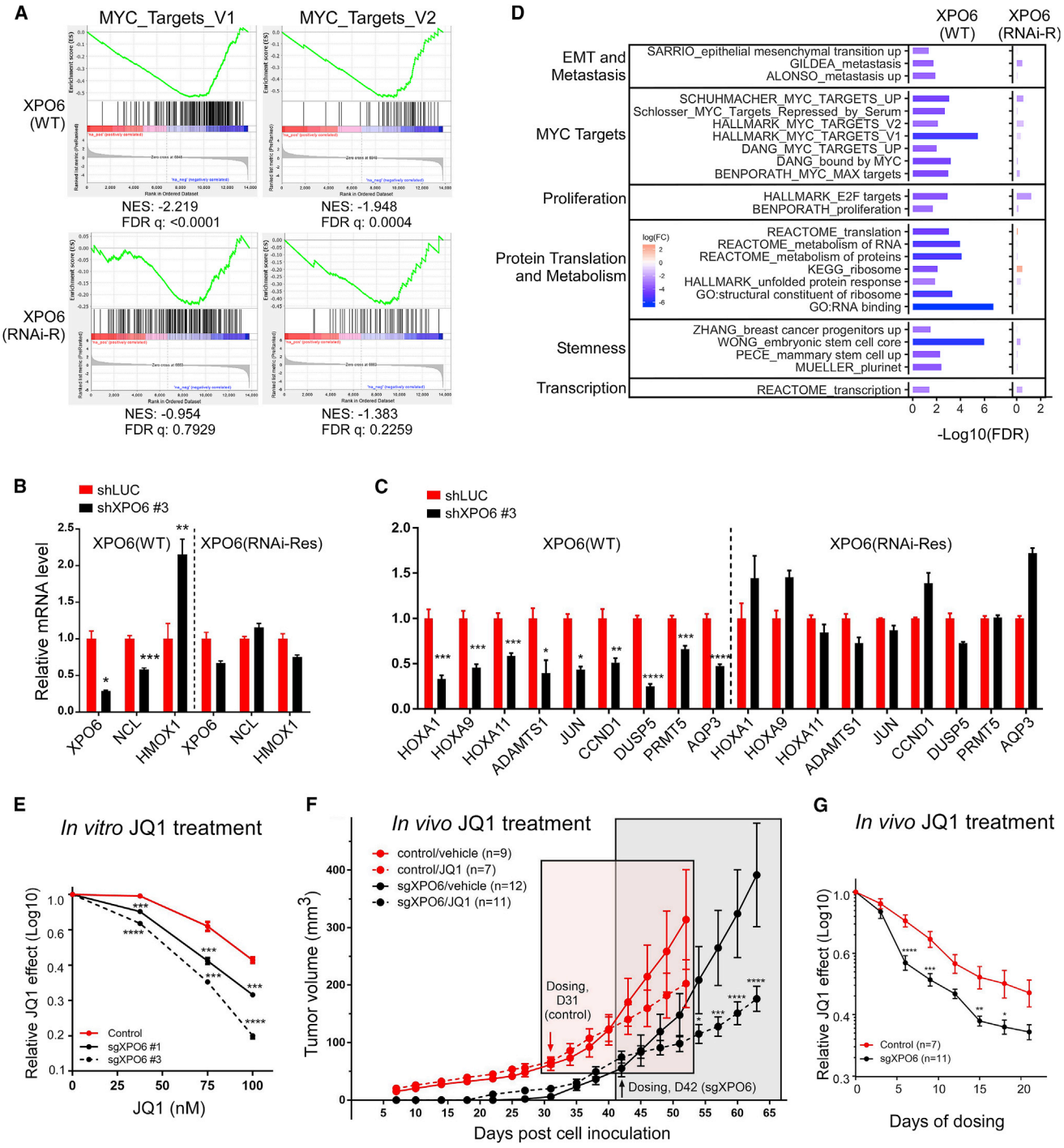


**Figure 7. XPO6 loss triggers anticancer transcriptomic effects and sensitization to BET inhibitor JQ1**

(A) RNA-seq using shLUC- or shXPO6-#3-infected MCF-7 cells expressing XPO6(WT) or XPO6(RNAi-Res). GSEA evaluating changes in the 50 hallmark gene sets induced by XPO6 knockdown. Shown are MYC targets V1 and V2 gene sets.

(B and C) qRT-PCR validation of DE genes induced by XPO6 knockdown specifically in MCF-7 cells expressing XPO6(WT) but not XPO6(RNAi-Res). (B) XPO6 and MYC target genes *NCL* (activated) and *HMOX1* (repressed) were analyzed. (C) Various known SEC target genes were analyzed. p values were based on unpaired t test by comparing shLUC versus shXPO6 for each gene.

(D) Representative gene sets significantly enriched by XPO6 knockdown in MCF-7 cells expressing XPO6(WT) but not XPO6(RNAi-Res). Analysis was performed using R/GAGE against GO molecular functions and multiple curated MSigDB databases (hallmark, KEGG, Reactome, Chemical and Genetic Perturbation) and graphed by R/ggplot2.

*(legend continued on next page)*

for *XPO6* and *MYC* range from 0.1 to 0.46. The ρ for breast cancer is 0.15, ranking *XPO6* within the top 16% of all genes positively correlated with *MYC* (Figure S7D). As a control, we detected positive correlations between *MYC* and *BRD4* (positive regulator of *MYC*) in 28 out of 32 tumor types, with 15 being statistically significant (Figure 6G). Correlation coefficients for *MYC* and *BRD4* range from 0.1 to 0.41, comparable to those for *MYC* and *XPO6* (Table S3). As an additional control, we detected positive correlations between *MYC* and its target gene *NCL* in all 32 tumor types, with 30 being statistically significant (ρ, 0.04–0.67) (Figure 6G; Table S3).

Next, we performed chromatin IP (ChIP) using MCF-7 cells to determine whether the inhibitory effect of nuclear Pfn1 on *MYC* transcription was due to decreased chromatin occupancy of SEC. Using antibodies for ENL, Cdk9, and cyclin T1 and *MYC*-specific primers (He et al., 2011), we detected significant inhibition of chromatin occupancy of the SEC by both NLS-Pfn1(WT) and XPO6 knockdown (Figures 6H and 6I). Consistent with the importance of PLP binding in Pfn1/SEC interaction, NLS-Pfn1(S137D) failed to inhibit SEC chromatin occupancy. Instead, it increased SEC occupancy at the *MYC* gene locus, mirroring its effect on *MYC* mRNA levels and indicating a dominant-negative effect. Since the SEC promotes gene transcription by phosphorylating $Ser^2$ of Rpb1, we performed ChIP for p-Rpb1($Ser^2$). Reduced p-Rpb1($Ser^2$) levels were observed at the *MYC* locus by NLS-Pfn1(WT) expression and XPO6 knockdown (Figures 6H and 6I). The inhibitory effect of nuclear Pfn1 on *MYC* occupancy of the SEC and p-Rpb1($Ser^2$) was similarly induced by untagged Pfn1 in a PLP-binding dependent fashion (Figure S7E). Conversely, Pfn1 knockdown increased *MYC* occupancy of the SEC and p-Rpb1($Ser^2$) (Figure S7F). Further, H3K36me3, a positive transcriptional marker depending on transcriptional elongation by p-Rpb1($Ser^2$) (Edmunds et al., 2008), was significantly decreased at the *MYC* locus by NLS-Pfn1(WT) and XPO6 knockdown (Figures 6H and 6I). These data suggest that nuclear Pfn1, increased by XPO6 loss, inhibits the transcription of *MYC* by blocking chromatin recruitment of SEC and the consequent $Ser^2$ phosphorylation of RNA Pol II necessary for transcription elongation.

## XPO6 loss triggers anticancer transcriptomic changes and sensitization to BET inhibition

To understand the broader transcriptional impact of nuclear Pfn1, we performed RNA-seq using XPO6 knockdown/rescue MCF-7 cells. We first performed gene set enrichment analysis (GSEA) using the differential expression values (fold change of shXPO6 versus shLUC) of all detected genes in XPO6(WT) or XPO6(RNAi-Res) cells. Using the well-annotated hallmark gene sets in the Molecular Signatures Database (MSigDB), we observed significant enrichment in nine gene sets (Figures 7A, S8A, and S9; Table S4A). Notably, all nine gene sets are negatively enriched by XPO6 knockdown, reflecting gene downregulation, and insignificant in the XPO6(RNAi-Res) cells (Figures 7A, S8A, and S9; Table S4A), confirming that the effects are due to XPO6 loss. Among them, the first and third highest-ranked gene sets by normalized enrichment score are MYC targets V1 and V2. We further confirmed this by examining the transcript levels of *NCL*, a known MYC-activated gene, and *HMOX1*, a known MYC-repressed gene, which were inhibited and promoted by XPO6 knockdown, respectively (Figure 7B). In addition to MYC targets, reduced expression of multiple known SEC target genes (Lin et al., 2011; Luo et al., 2012a) as a result of XPO6 knockdown in XPO6(WT) but not XPO6(RNAi-Res) cells was detected by RNA-seq and validated by qRT-PCR (Figure 7C). The additional hallmark gene sets in which shXPO6-induced differentially expressed (DE) genes were negatively enriched include E2F targets, epithelial mesenchymal transition, unfolded protein response, MTORC1 signaling, oxidative phosphorylation, reactive oxygen species pathways, and adipogenesis, all of which were rescued by XPO6(RNAi-Res) (Figures S8A and S9; Table S4A). This indicates that XPO6 loss inhibits a multitude of cancer-driving processes related to proliferation, metastasis, and metabolism.

To investigate this further, we performed pathway analyses for statistically significant shXPO6-induced DE genes (adjusted p value < 0.05). Using Gene Ontology (GO) and several MSigDB gene sets, we detected, specifically in the XPO6(WT) cells, statistically significant downregulation of five additional MYC target gene sets besides the two hallmark MYC targets V1 and V2 (Figure 7D). Consistent with the GSEA results, we also detected significant downregulation of multiple gene sets related to proliferation, metastasis, transcription, and translation (Figure 7D; Table S4B). In addition, we detected significant downregulation of multiple stem-cell-related gene sets and EZH2-stimulated genes, accompanied by the upregulation of EZH2-repressed genes bearing the H3K27me3 mark (Figure S8B). Thus, XPO6 loss triggers transcriptomic changes indicative of the suppression of multiple phenotypic aspects of cancer.

The SEC and BET families of bromodomain-containing proteins have similar functions in promoting oncogenic transcription by independently binding p-TEFb and phosphorylating $Ser^2$ of RNA Pol II. It was recently reported that SEC inhibition via ENL

(E) MDA-MB-231 cells infected with control or sgXPO6 viruses were treated with DMSO or JQ1 in colony formation assays for 10 days. p values were based on one-way ANOVA and Dunnett's multiple comparisons by comparing control and sgXPO6 cells at different JQ1 concentrations. Data in (B), (C), and (E) are mean ± SEM of representative experiments (triplicates per condition) and were confirmed three times.

(F) MDA-MB-231 cells from (E) were orthotopically injected into female nude mice and treated with vehicle or JQ1 for 3 weeks. Mice in the sgXPO6 #1 and #3 groups were combined for analysis. Arrows indicate treatment start dates. p values were based on two-way ANOVA and Sidak's multiple comparison tests to compare vehicle versus JQ1 groups.

(G) Relative growth rates of individual tumors during the dosing period were first calculated by dividing tumor volumes at various time points by day 1. The calculated tumor growth rates in the JQ1 groups of control or sgXPO6 mice were subsequently divided by the averaged growth rates of the corresponding vehicle groups, giving rise to the relative JQ effect (y axis).

p values were based on two-way ANOVA and Sidak's multiple comparison tests. *p < 0.05; **p < 0.01; ***p < 0.001; ****p < 0.0001. See also Figures S8–S10 and Table S4.

deletion sensitizes leukemia cells to the BET inhibitor JQ1 (Wan et al., 2017). Since nuclear Pfn1 inhibits SEC function, we asked whether it could sensitize cancer cells to JQ1. Indeed, XPO6 knockdown (Figure S10A) and KO (Cas9n, Figure S10B; Cas9, Figure 7E) both rendered the triple-negative MDA-MB-231 cells, known to depend on Brd4 function, more sensitive to JQ1 *in vitro*. To confirm this *in vivo*, we orthotopically injected MDA-MB-231 cells infected with control or two different sgXPO6 viruses in female nude mice. When the average tumor volumes in each group reached ~70 $mm^3$, we randomly divided and treated them daily with vehicle or JQ1 for 3 weeks. Control cells formed tumors significantly faster (by 2 weeks) at a higher frequency (90% versus 50% of injection sites) than the *XPO6* KO cells (Figure 7F). Because of the low tumor take rate of *XPO6* KO cells, the two sgXPO6 groups were combined for data analysis to increase statistical power. Statistically significant tumor inhibition by JQ1 was observed at multiple time points post-treatment in the sgXPO6 group but not the control group (Figure 7F), and the relative difference in tumor volumes between JQ1 and vehicle-treated mice was significantly larger in the sgXPO6 group than the control group (Figure 7G). Notably, XPO6 protein levels remained low in the resected tumors of the sgXPO6 groups but visibly higher than the levels prior to mouse inoculation (Figures S10C and S10D). This indicates a selection pressure during *in vivo* expansion to restore XPO6 expression or the amplification of a small fraction of tumor cells with inefficient *XPO6* KO. Regardless, our data demonstrate that in addition to being a therapeutic target on its own, XPO6 may be inhibited to enhance the anticancer efficacy of BET inhibitors.

## DISCUSSION

An emerging paradigm of non-oncogene addiction in cancer is altered nucleocytoplasmic protein trafficking caused by aberrant expression of nuclear transporters. Here, we focused on the highly selective nuclear exporter XPO6, whose only known cargo is the dimeric actin/Pfn complex (Stüven et al., 2003). Despite the largely unexplored role of XPO6 in cancer, we were intrigued by the long-standing paradox regarding the opposing cellular functions of its cargo Pfn1. Although the essentiality of Pfn1 explains the extreme rarity of its loss-of-function mutations in cancer, both its clinical relevance and anticancer mechanism remain poorly defined. Adding to the complexity are the inconsistent patterns of Pfn1 expression changes in cancer. Our earlier report indicated that cell nucleus might be the spatial origin of Pfn1's anticancer function (Diamond et al., 2015). Work in this paper supports this theory and suggests that Pfn1 is deregulated in cancer primarily on the protein level through nuclear exclusion caused by XPO6 upregulation. This model not only reconciles the paradoxical Pfn1 functions that co-exist in normal cells, but also explains how cancer cells can specifically inhibit the anticancer activity of Pfn1 without compromising its essential cytoplasmic function.

By analyzing publicly available human cancer data, we detected widespread upregulation of *XPO6* mRNA within numerous tumor types. For breast cancer, this does not depend on stage or subtype, indicating that XPO6 upregulation may be an early and prevalent cancer-associated event. High levels of *XPO6* mRNA and protein correlate with poor breast cancer survival. Interestingly, our analyses suggested that XPO6 level is preferentially associated with the survival of lymph-node-positive breast cancer patients. While this implies a greater impact of XPO6 on invasive breast cancer, we did not observe a correlation between XPO6 and breast cancer progression using the TCGA dataset. Nonetheless, this possibility may be further tested in the future using independent datasets.

In support of patient data, we showed that XPO6 loss caused growth inhibition of multiple breast cancer cell lines, regardless of subtype, and two sarcoma cell lines *in vitro*. This was confirmed *in vivo* using orthotopically implanted MCF-7 cells. In our experimental systems, cell-cycle inhibition appears to be a major factor underlying the anticancer effect of XPO6 loss. This supports prior findings that Pfn1, the cargo of XPO6, causes cell-cycle arrest in breast cancer cells (Diamond et al., 2015; Zou et al., 2010). Intriguingly, XPO6 loss did not trigger detectable growth inhibition of the untransformed mammary epithelial MCF10A cells. However, the growth inhibition by XPO6 knockdown in the mouse chondrocytes indicates that tolerability of XPO6 inhibition by healthy cells may depend on their tissue origins and contexts. This will be an important question to address in future studies.

By discovering the interaction between Pfn1 and the SEC, we defined a molecular function of nuclear Pfn1 and linked it directly to cancer. The SEC has been extensively studied for its role in productive transcriptional elongation (He et al., 2010; Lin et al., 2010; Sobhian et al., 2010). Its cancer relevance has long been implicated by the frequent fusion between its different components and the *MLL* oncogene in childhood leukemia. A recent study showed that *MLLT1* (encoding ENL) mutations are causally linked to Wilms tumors (Perlman et al., 2015). Even in the absence of genetic aberrations, the SEC is important for cancer due to its positive regulation of processive transcription of various pro-cancer genes, most notably *MYC* (Liang et al., 2018). ENL was recently identified as an acetyl-lysine-binding protein, joining the BET family proteins as an epigenetic reader (Wan et al., 2017). This supports the idea that the SEC and BET proteins play similar, albeit non-identical, roles in recruiting p-TEFb to acetylated chromatin regions to drive transcription. This is consistent with the finding that ENL depletion in leukemia cells inhibited Cdk9 chromatin recruitment (Wan et al., 2017). As for negative regulators of p-TEFb, for nearly two decades the 7SK small nuclear ribonucleoprotein (snRNP) complex remains its only known inhibitor (Nguyen et al., 2001; Yang et al., 2001). However, it is unknown whether p-TEFb can be inhibited outside of 7SK snRNP, especially when it is bound with positive regulators. We show that nuclear Pfn1 interacts with the SEC, via direct binding to the PLP motif in ENL, and reduces SEC chromatin occupancy at the *MYC* locus. This is associated with decreased levels of p-Rpb1($Ser^2$) (indicative of lower p-TEFb activity) at the *MYC* gene locus and downregulation of its expression. Interestingly, separate SECs exist containing either ENL or AF9 that occupy the same region in the scaffold protein AFF4. The absence of a PLP motif in AF9 may explain why it was not detected as a binding partner of nuclear Pfn1. Thus, we have identified nuclear Pfn1 as a negative regulator of p-TEFb in the context of ENL-containing SEC.

Consistent with our hypothesis that the pro-cancer effect of XPO6 stems from its ability to reduce nuclear Pfn1 level, XPO6 loss causes a similar inhibition of SEC occupancy at the *MYC* gene locus and *MYC* expression. Importantly, both the inhibitory effects of XPO6 loss on *MYC* expression and cancer cell growth are abolished when Pfn1 is absent, suggesting that it is the nuclear accumulation of Pfn1, rather than actin, that underlies these effects. This is consistent with the positive regulation of general transcription by nuclear actin (Virtanen and Vartiainen, 2017). In fact, in *Pfn1*-null mouse chondrocytes, XPO6 loss causes a small, but reproducible, increase in *MYC* expression and cell growth. Since actin can be exported by XPO6, albeit less efficiently, in the absence of Pfn1, this functionally separates nuclear Pfn1 and actin with regard to their roles in gene regulation. The inhibitory effect of XPO6 loss on the SEC was further confirmed by genome-wide transcriptomic analysis, which showed significant downregulation of multiple MYC target gene sets and known SEC target genes. Since the SEC both promotes *MYC* expression as a target gene (Luo et al., 2012a) and functionally collaborates with MYC as a transcription factor (Liang et al., 2018), the mechanism behind the inhibition of MYC target genes by nuclear Pfn1 could be 2-fold. The significant downregulation of genes involved in proliferation (e.g., E2F targets) and metastasis (e.g., EMT) by XPO6 loss is consistent with the known anti-proliferative and anti-metastatic effects of Pfn1 in different tumor models and suggests that these effects originate, at least partially, from its nuclear function as an inhibitor of SEC-dependent transcription. It was intriguing to observe the significant downregulation of additional gene sets, as a result of XPO6 loss, that are functionally associated with diverse cellular processes including protein translation, oxidative phosphorylation, and adipogenesis as well as those associated with reactive oxygen species pathways and stem cell signatures, all of which have been positively linked to MYC activation (Meyer and Penn, 2008). Consistent with the role of the SEC as a transcriptional activator, nearly all the significantly enriched gene sets and biological pathways represent downregulated genes due to XPO6 loss. The only notable exception was an upregulation of two H3K27me3 gene sets representing repressed target genes of the oncogenic histone methyltransferase EZH2, which coincide with a downregulation of its activated target genes. It was previously shown that MYC stimulates *EZH2* expression both transcriptionally as a target gene and post-transcriptionally by repressing its negative regulator miR-26 (Sander et al., 2008). Thus, the effect of XPO6 loss on EZH2 function may be similarly, and at least partially, caused by MYC repression due to SEC inhibition.

The diverse transcriptional effects and robust antitumor effects triggered by XPO6 loss provide orthogonal validation of recent findings that targeting the SEC, either by ENL deletion (Erb et al., 2017; Wan et al., 2017) or by disrupting AFF4/CycT1 interaction (Liang et al., 2018), achieved significant anticancer effects. Among various therapeutic implications, the parallel functions of ENL (in the context of the SEC) and BET proteins as acetyllysine-specific epigenetic readers motivated us to test the influence of XPO6 loss on the anticancer effects of JQ1. Consistent with a recent report that ENL depletion sensitizes leukemia cells to JQ1 (Wan et al., 2017), we observed increased growth inhibition by JQ1 of the triple-negative breast cancer cell line MDA-MB-231 with XPO6 loss. Given the intensive efforts to find synthetic lethal partners of BET proteins to more effectively treat cancer (Shu et al., 2016), our data provide important proof-of-concept that XPO6 may be a potentially useful target in this regard.

In summary, we discovered that XPO6 upregulation is a previously unrecognized cancer driver event. By finding that nuclear Pfn1, the cargo of XPO6, is a physical binding partner and functional inhibitor of the SEC, we defined a moonlighting function of nuclear Pfn1 in transcriptional repression that is mechanistically linked to its poorly understood anticancer function. Our work highlights the importance of subcellular localization in protein function and the oncogenic effects of protein spatial deregulation that may arise due to aberrant expression of nucleocytoplasmic transporters. Future studies to expand our knowledge of spatially dynamic, multi-functional proteins such as Pfn1 are warranted and will likely unveil hidden biology, as well as therapeutic opportunities to treat cancer.

## STAR★METHODS

Detailed methods are provided in the online version of this paper and include the following:

- KEY RESOURCES TABLE
- RESOURCE AVAILABILITY
  - Lead contact
  - Materials availability
  - Data and code availability
- EXPERIMENTAL MODEL AND SUBJECT DETAILS
  - Cell lines
  - Animal experiments
- METHOD DETAILS
  - Antibodies
  - Plasmids, shRNAs, and sgRNAs
  - CRISPR/Cas9 editing
  - *In vitro* growth assays
  - Cell cycle analysis
  - Co-immunoprecipitation and mass spectrometry
  - Co-immunoprecipitation and western blot
  - Size exclusion chromatography
  - BrdU labeling
  - Immunofluorescence staining, cell imaging, and nuclear/cytoplasmic intensity analysis
  - Immunohistochemistry
  - qRT-PCR
  - ChIP-qPCR
  - RNA-seq
- QUANTIFICATION AND STATISTICAL ANALYSIS
  - TCGA gene expression analyses
  - Combined TCGA/GTEx gene expression analyses
  - CPTAC proteomic data analysis
  - Kaplan-Meier survival analyses
  - RNA-seq analysis

## SUPPLEMENTAL INFORMATION

Supplemental information can be found online at https://doi.org/10.1016/j.celrep.2021.108749.

## ACKNOWLEDGMENTS

We thank Dr. Jason Weber and Dr. Brian Van Tine for providing HUMEC and sarcoma cell lines. We thank Dr. Ralph T. Bottcher and Dr. Reinhard Fassler (Max Planck Institute of Biochemistry, Germany) for providing the *Pfn1*-null mouse chondrocytes. We thank Dr. Shunqiang Li and Tina Primeau for assistance with tumor section. We thank Dr. Kian-Huat Lim for sharing the pSpCas9n(BB)-2A-Puro and LentiCRISPRv2 vectors. We thank Dr. Jingqin Luo for statistical advice. The monoclonal GFP antibody was purchased from the Developmental Studies Hybridoma Bank, created by the NICHD of the NIH and maintained at The University of Iowa. We thank the Genome Technology Access Center at Washington University for performing RNA-seq. We thank the Alvin J. Siteman Cancer Center, Barnes-Jewish Hospital, and the Institute of Clinical and Translational Sciences (ICTS) at Washington University for the use of the Proteomics Shared Resource and the Flow Cytometry core. The Siteman Cancer Center is supported in part by an NCI Cancer Center support grant P30 CA091842, and the ICTS is funded by the National Institutes of Health's NCATS Clinical and Translational Science Award (CTSA) program grant UL1 TR002345. Transcriptomic and proteomic data used in this publication were generated by The Cancer Genome Atlas and Clinical Proteomic Tumor Analysis Consortium (NCI/NIH). This study was partially supported by the Susan G. Komen Foundation (J.S., CCR14300139), National Cancer Institute (J.S., 5R01CA181671; E.M.O., CA188286), and National Institute of Allergy and Infectious Diseases (E.M.O., AI118852). F.W. was supported by the National Natural Science Foundation of China (81801939).

## AUTHOR CONTRIBUTIONS

J.S. conceived the project and wrote the manuscript with input from all authors. J.S., C.Z., and S.-J.K. designed the experiments. J.S., C.Z., S.-J.K., F.W., S.H., Z.L., Z.G., and J.M.H. performed the experiments and analyzed the data. A.M. and K.W. performed bioinformatics analysis. J.M.H., C.X.M., P.L.C., and E.M.O. provided technical expertise and intellectual input.

## DECLARATION OF INTERESTS

No authors declare no competing interests.

Received: March 8, 2020
Revised: December 29, 2020
Accepted: January 21, 2021
Published: February 16, 2021

## REFERENCES

Balasubramanian, M.K., Hirani, B.R., Burke, J.D., and Gould, K.L. (1994). The Schizosaccharomyces pombe cdc3+ gene encodes a profilin essential for cytokinesis. J. Cell Biol. *125*, 1289–1301.

Bohnsack, M.T., Stüven, T., Kuhn, C., Cordes, V.C., and Görlich, D. (2006). A selective block of nuclear actin export stabilizes the giant nuclei of Xenopus oocytes. Nat. Cell Biol. *8*, 257–263.

Böttcher, R.T., Wiesner, S., Braun, A., Wimmer, R., Berna, A., Elad, N., Medalia, O., Pfeifer, A., Aszódi, A., Costell, M., and Fässler, R. (2009). Profilin 1 is required for abscission during late cytokinesis of chondrocytes. EMBO J. *28*, 1157–1169.

Carlsson, L., Nyström, L.E., Sundkvist, I., Markey, F., and Lindberg, U. (1977). Actin polymerizability is influenced by profilin, a low molecular weight protein in non-muscle cells. J. Mol. Biol. *115*, 465–483.

Cox, J., and Mann, M. (2008). MaxQuant enables high peptide identification rates, individualized p.p.b.-range mass accuracies and proteome-wide protein quantification. Nat. Biotechnol. *26*, 1367–1372.

Diamond, M.I., Cai, S., Boudreau, A., Carey, C.J., Jr., Lyle, N., Pappu, R.V., Swamidass, S.J., Bissell, M., Piwnica-Worms, H., and Shao, J. (2015). Subcellular localization and Ser-137 phosphorylation regulate tumor-suppressive activity of profilin-1. J. Biol. Chem. *290*, 9075–9086.

Edmunds, J.W., Mahadevan, L.C., and Clayton, A.L. (2008). Dynamic histone H3 methylation during gene induction: HYPB/Setd2 mediates all H3K36 trimethylation. EMBO J. *27*, 406–420.

Erb, M.A., Scott, T.G., Li, B.E., Xie, H., Paulk, J., Seo, H.S., Souza, A., Roberts, J.M., Dastjerdi, S., Buckley, D.L., et al. (2017). Transcription control by the ENL YEATS domain in acute leukaemia. Nature *543*, 270–274.

Erde, J., Loo, R.R., and Loo, J.A. (2014). Enhanced FASP (eFASP) to increase proteome coverage and sample recovery for quantitative proteomic experiments. J. Proteome Res. *13*, 1885–1895.

Finetti, P., Cervera, N., Charafe-Jauffret, E., Chabannon, C., Charpin, C., Chaffanet, M., Jacquemier, J., Viens, P., Birnbaum, D., and Bertucci, F. (2008). Sixteen-kinase gene expression identifies luminal breast cancers with poor prognosis. Cancer Res. *68*, 767–776.

Fox, A.H., and Lamond, A.I. (2010). Paraspeckles. Cold Spring Harb. Perspect. Biol. *2*, a000687.

Gandhi, U.H., Senapedis, W., Baloglu, E., Unger, T.J., Chari, A., Vogl, D., and Cornell, R.F. (2018). Clinical Implications of Targeting XPO1-mediated Nuclear Export in Multiple Myeloma. Clin. Lymphoma Myeloma Leuk. *18*, 335–345.

Giesemann, T., Rathke-Hartlieb, S., Rothkegel, M., Bartsch, J.W., Buchmeier, S., Jockusch, B.M., and Jockusch, H. (1999). A role for polyproline motifs in the spinal muscular atrophy protein SMN. Profilins bind to and colocalize with smn in nuclear gems. J. Biol. Chem. *274*, 37908–37914.

Gravina, G.L., Senapedis, W., McCauley, D., Baloglu, E., Shacham, S., and Festuccia, C. (2014). Nucleo-cytoplasmic transport as a therapeutic target of cancer. J. Hematol. Oncol. *7*, 85.

Güttler, T., and Görlich, D. (2011). Ran-dependent nuclear export mediators: a structural perspective. EMBO J. *30*, 3457–3474.

Hao, J., Chiang, Y.T., Gout, P.W., and Wang, Y. (2016). Elevated XPO6 expression as a potential prognostic biomarker for prostate cancer recurrence. Front. Biosci. (Schol. *8*, 44–55.

He, N., Liu, M., Hsu, J., Xue, Y., Chou, S., Burlingame, A., Krogan, N.J., Alber, T., and Zhou, Q. (2010). HIV-1 Tat and host AFF4 recruit two transcription elongation factors into a bifunctional complex for coordinated activation of HIV-1 transcription. Mol. Cell *38*, 428–438.

He, N., Chan, C.K., Sobhian, B., Chou, S., Xue, Y., Liu, M., Alber, T., Benkirane, M., and Zhou, Q. (2011). Human Polymerase-Associated Factor complex (PAFc) connects the Super Elongation Complex (SEC) to RNA polymerase II on chromatin. Proc. Natl. Acad. Sci. USA *108*, E636–E645.

Higgs, M.R., Reynolds, J.J., Winczura, A., Blackford, A.N., Borel, V., Miller, E.S., Zlatanou, A., Nieminuszczy, J., Ryan, E.L., Davies, N.J., et al. (2015). BOD1L Is Required to Suppress Deleterious Resection of Stressed Replication Forks. Mol. Cell *59*, 462–477.

Holt, M.R., and Koffer, A. (2001). Cell motility: proline-rich proteins promote protrusions. Trends Cell Biol. *11*, 38–46.

Hung, M.C., and Link, W. (2011). Protein localization in disease and therapy. J. Cell Sci. *124*, 3381–3392.

Jockusch, B.M., Murk, K., and Rothkegel, M. (2007). The profile of profilins. Rev. Physiol. Biochem. Pharmacol. *159*, 131–149.

Kalakonda, N., Maerevoet, M., Cavallo, F., Follows, G., Goy, A., Vermaat, J.S.P., Casasnovas, O., Hamad, N., Zijlstra, J.M., Bakhshi, S., et al. (2020). Selinexor in patients with relapsed or refractory diffuse large B-cell lymphoma (SADAL): a single-arm, multinational, multicentre, open-label, phase 2 trial. Lancet Haematol. *7*, e511–e522.

Kim, E., Tyagi, R., Lee, J.Y., Park, J., Kim, Y.R., Beon, J., Chen, P.Y., Cha, J.Y., Snyder, S.H., and Kim, S. (2013). Inositol polyphosphate multikinase is a coactivator for serum response factor-dependent induction of immediate early genes. Proc. Natl. Acad. Sci. USA *110*, 19938–19943.

Lederer, M., Jockusch, B.M., and Rothkegel, M. (2005). Profilin regulates the activity of p42POP, a novel Myb-related transcription factor. J. Cell Sci. *118*, 331–341.

Li, B., and Dewey, C.N. (2011). RSEM: accurate transcript quantification from RNA-Seq data with or without a reference genome. BMC Bioinformatics *12*, 323.

Liang, K., Smith, E.R., Aoi, Y., Stoltz, K.L., Katagi, H., Woodfin, A.R., Rendleman, E.J., Marshall, S.A., Murray, D.C., Wang, L., et al. (2018). Targeting Processive Transcription Elongation via SEC Disruption for MYC-Induced Cancer Therapy. Cell *175*, 766–779.e17.

Lin, C., Smith, E.R., Takahashi, H., Lai, K.C., Martin-Brown, S., Florens, L., Washburn, M.P., Conaway, J.W., Conaway, R.C., and Shilatifard, A. (2010). AFF4, a component of the ELL/P-TEFb elongation complex and a shared subunit of MLL chimeras, can link transcription elongation to leukemia. Mol. Cell *37*, 429–437.

Lin, C., Garrett, A.S., De Kumar, B., Smith, E.R., Gogol, M., Seidel, C., Krumlauf, R., and Shilatifard, A. (2011). Dynamic transcriptional events in embryonic stem cells mediated by the super elongation complex (SEC). Genes Dev. *25*, 1486–1498.

Liu, J., Lichtenberg, T., Hoadley, K.A., Poisson, L.M., Lazar, A.J., Cherniack, A.D., Kovatich, A.J., Benz, C.C., Levine, D.A., Lee, A.V., et al.; Cancer Genome Atlas Research Network (2018). An Integrated TCGA Pan-Cancer Clinical Data Resource to Drive High-Quality Survival Outcome Analytics. Cell *173*, 400–416.e11.

Loi, S., Haibe-Kains, B., Desmedt, C., Wirapati, P., Lallemand, F., Tutt, A.M., Gillet, C., Ellis, P., Ryder, K., Reid, J.F., et al. (2008). Predicting prognosis using molecular profiling in estrogen receptor-positive breast cancer treated with tamoxifen. BMC Genomics *9*, 239.

Luo, Z., Lin, C., Guest, E., Garrett, A.S., Mohaghegh, N., Swanson, S., Marshall, S., Florens, L., Washburn, M.P., and Shilatifard, A. (2012a). The super elongation complex family of RNA polymerase II elongation factors: gene target specificity and transcriptional output. Mol. Cell. Biol. *32*, 2608–2617.

Luo, Z., Lin, C., and Shilatifard, A. (2012b). The super elongation complex (SEC) family in transcriptional control. Nat. Rev. Mol. Cell Biol. *13*, 543–547.

Mahipal, A., and Malafa, M. (2016). Importins and exportins as therapeutic targets in cancer. Pharmacol. Ther. *164*, 135–143.

McLaughlin-Drubin, M.E., Crum, C.P., and Münger, K. (2011). Human papillomavirus E7 oncoprotein induces KDM6A and KDM6B histone demethylase expression and causes epigenetic reprogramming. Proc. Natl. Acad. Sci. USA *108*, 2130–2135.

Méndez, J., and Stillman, B. (2000). Chromatin association of human origin recognition complex, cdc6, and minichromosome maintenance proteins during the cell cycle: assembly of prereplication complexes in late mitosis. Mol. Cell. Biol. *20*, 8602–8612.

Meyer, N., and Penn, L.Z. (2008). Reflecting on 25 years with MYC. Nat. Rev. Cancer *8*, 976–990.

Nagy, Á., Lánczky, A., Menyhárt, O., and Győrffy, B. (2018). Validation of miRNA prognostic power in hepatocellular carcinoma using expression data of independent datasets. Sci. Rep. *8*, 9227.

Nguyen, V.T., Kiss, T., Michels, A.A., and Bensaude, O. (2001). 7SK small nuclear RNA binds to and inhibits the activity of CDK9/cyclin T complexes. Nature *414*, 322–325.

Park, S.H., Park, T.J., and Lim, I.K. (2011). Reduction of exportin 6 activity leads to actin accumulation via failure of RanGTP restoration and NTF2 sequestration in the nuclei of senescent cells. Exp. Cell Res. *317*, 941–954.

Perlman, E.J., Gadd, S., Arold, S.T., Radhakrishnan, A., Gerhard, D.S., Jennings, L., Huff, V., Guidry Auvil, J.M., Davidsen, T.M., Dome, J.S., et al. (2015). MLLT1 YEATS domain mutations in clinically distinctive Favourable Histology Wilms tumours. Nat. Commun. *6*, 10013.

Perrimon, N., Engstrom, L., and Mahowald, A.P. (1989). Zygotic lethals with specific maternal effect phenotypes in Drosophila melanogaster. I. Loci on the X chromosome. Genetics *121*, 333–352.

Ran, F.A., Hsu, P.D., Wright, J., Agarwala, V., Scott, D.A., and Zhang, F. (2013). Genome engineering using the CRISPR-Cas9 system. Nat. Protoc. *8*, 2281–2308.

Rengasamy, M., Zhang, F., Vashisht, A., Song, W.M., Aguilo, F., Sun, Y., Li, S., Zhang, W., Zhang, B., Wohlschlegel, J.A., and Walsh, M.J. (2017). The PRMT5/WDR77 complex regulates alternative splicing through ZNF326 in breast cancer. Nucleic Acids Res. *45*, 11106–11120.

Robinson, J.T., Thorvaldsdóttir, H., Winckler, W., Guttman, M., Lander, E.S., Getz, G., and Mesirov, J.P. (2011). Integrative genomics viewer. Nat. Biotechnol. *29*, 24–26.

Sander, S., Bullinger, L., Klapproth, K., Fiedler, K., Kestler, H.A., Barth, T.F., Möller, P., Stilgenbauer, S., Pollack, J.R., and Wirth, T. (2008). MYC stimulates EZH2 expression by repression of its negative regulator miR-26a. Blood *112*, 4202–4212.

Shu, S., Lin, C.Y., He, H.H., Witwicki, R.M., Tabassum, D.P., Roberts, J.M., Janiszewska, M., Huh, S.J., Liang, Y., Ryan, J., et al. (2016). Response and resistance to BET bromodomain inhibitors in triple-negative breast cancer. Nature *529*, 413–417.

Skare, P., Kreivi, J.P., Bergström, A., and Karlsson, R. (2003). Profilin I colocalizes with speckles and Cajal bodies: a possible role in pre-mRNA splicing. Exp. Cell Res. *286*, 12–21.

Sobhian, B., Laguette, N., Yatim, A., Nakamura, M., Levy, Y., Kiernan, R., and Benkirane, M. (2010). HIV-1 Tat assembles a multifunctional transcription elongation complex and stably associates with the 7SK snRNP. Mol. Cell *38*, 439–451.

Spencer, V.A., Costes, S., Inman, J.L., Xu, R., Chen, J., Hendzel, M.J., and Bissell, M.J. (2011). Depletion of nuclear actin is a key mediator of quiescence in epithelial cells. J. Cell Sci. *124*, 123–132.

Struntz, N.B., Chen, A., Deutzmann, A., Wilson, R.M., Stefan, E., Evans, H.L., Ramirez, M.A., Liang, T., Caballero, F., Wildschut, M.H.E., et al. (2019). Stabilization of the Max Homodimer with a Small Molecule Attenuates Myc-Driven Transcription. Cell Chem. Biol. *26*, 711–723.e14.

Stüven, T., Hartmann, E., and Görlich, D. (2003). Exportin 6: a novel nuclear export receptor that is specific for profilin.actin complexes. EMBO J. *22*, 5928–5940.

Subramanian, A., Tamayo, P., Mootha, V.K., Mukherjee, S., Ebert, B.L., Gillette, M.A., Paulovich, A., Pomeroy, S.L., Golub, T.R., Lander, E.S., and Mesirov, J.P. (2005). Gene set enrichment analysis: a knowledge-based approach for interpreting genome-wide expression profiles. Proc. Natl. Acad. Sci. USA *102*, 15545–15550.

Tang, W., Zhou, M., Dorsey, T.H., Prieto, D.A., Wang, X.W., Ruppin, E., Veenstra, T.D., and Ambs, S. (2018). Integrated proteotranscriptomics of breast cancer reveals globally increased protein-mRNA concordance associated with subtypes and survival. Genome Med. *10*, 94.

Verheyen, E.M., and Cooley, L. (1994). Profilin mutations disrupt multiple actin-dependent processes during Drosophila development. Development *120*, 717–728.

Virtanen, J.A., and Vartiainen, M.K. (2017). Diverse functions for different forms of nuclear actin. Curr. Opin. Cell Biol. *46*, 33–38.

Wan, L., Wen, H., Li, Y., Lyu, J., Xi, Y., Hoshii, T., Joseph, J.K., Wang, X., Loh, Y.E., Erb, M.A., et al. (2017). ENL links histone acetylation to oncogenic gene expression in acute myeloid leukaemia. Nature *543*, 265–269.

Wang, Q., Armenia, J., Zhang, C., Penson, A.V., Reznik, E., Zhang, L., Minet, T., Ochoa, A., Gross, B.E., Iacobuzio-Donahue, C.A., et al. (2018). Unifying cancer and normal RNA sequencing data from different sources. Sci. Data *5*, 180061.

Wiśniewski, J.R., Zougman, A., Nagaraj, N., and Mann, M. (2009). Universal sample preparation method for proteome analysis. Nat. Methods *6*, 359–362.

Witke, W., Sutherland, J.D., Sharpe, A., Arai, M., and Kwiatkowski, D.J. (2001). Profilin I is essential for cell survival and cell division in early mouse development. Proc. Natl. Acad. Sci. USA *98*, 3832–3836.

Wittenmayer, N., Jandrig, B., Rothkegel, M., Schlüter, K., Arnold, W., Haensch, W., Scherneck, S., and Jockusch, B.M. (2004). Tumor suppressor activity of profilin requires a functional actin binding site. Mol. Biol. Cell *15*, 1600–1608.

Yang, Z., Zhu, Q., Luo, K., and Zhou, Q. (2001). The 7SK small nuclear RNA inhibits the CDK9/cyclin T1 kinase to control transcription. Nature *414*, 317–322.

Yao, W., Ji, S., Qin, Y., Yang, J., Xu, J., Zhang, B., Xu, W., Liu, J., Shi, S., Liu, L., et al. (2014). Profilin-1 suppresses tumorigenicity in pancreatic cancer through regulation of the SIRT3-HIF1$\alpha$ axis. Mol. Cancer *13*, 187.

Zhu, C., Rogers, A., Asleh, K., Won, J., Gao, D., Leung, S., Li, S., Vij, K.R., Zhu, J., Held, J.M., et al. (2020). Phospho-Ser$^{784}$-VCP Is Required for DNA Damage Response and Is Associated with Poor Prognosis of Chemotherapy-Treated Breast Cancer. Cell Rep. *31*, 107745.

Zoidakis, J., Makridakis, M., Zerefos, P.G., Bitsika, V., Esteban, S., Frantzi, M., Stravodimos, K., Anagnou, N.P., Roubelakis, M.G., Sanchez-Carbayo, M., and Vlahou, A. (2012). Profilin 1 is a potential biomarker for bladder cancer aggressiveness. Mol Cell Proteomics *11*, M111 009449.

Zou, L., Jaramillo, M., Whaley, D., Wells, A., Panchapakesa, V., Das, T., and Roy, P. (2007). Profilin-1 is a negative regulator of mammary carcinoma aggressiveness. Br. J. Cancer *97*, 1361–1371.

Zou, L., Ding, Z., and Roy, P. (2010). Profilin-1 overexpression inhibits proliferation of MDA-MB-231 breast cancer cells partly through p27kip1 upregulation. J. Cell. Physiol. *223*, 623–629.

## STAR★METHODS

### KEY RESOURCES TABLE

| REAGENT or RESOURCE | SOURCE | IDENTIFIER |
|---|---|---|
| **Antibodies** | | |
| rabbit anti-XPO6 | Thermo Fisher Scientific | Cat#: PA5-31813; RRID:AB_2549286 |
| mouse anti-RPb1(CTD) | Cell Signaling Technology | Cat#: 2629; RRID:AB_2167468 |
| rabbit anti-cyclin T1 | Cell Signaling Technology | Cat#: 81464; RRID:AB_2799973 |
| rabbit anti-Cdk9 | Cell Signaling Technology | Cat#: 2316; RRID:AB_2291505 |
| rabbit anti-GFP | Cell Signaling Technology | Cat#: 2956; RRID:AB_1196615 |
| rabbit anti-Histone H3 | Cell Signaling Technology | Cat#: 4499; RRID:AB_10544537 |
| rabbit anti-Pfn1 | Cell Signaling Technology | Cat#: 3237; RRID:AB_2236990 |
| rabbit anti-Pfn1 | Abcam | Cat#: ab124904; RRID:AB_10975882 |
| rabbit anti-Pfn1 | Sigma-Aldrich | Cat#: P7624; RRID:AB_1079598 |
| rat anti-GFP | BioLegend | Cat#: 338002; RRID:AB_1279414 |
| rabbit anti-ENL | Bethyl | Cat#: A302-268A; RRID:AB_1731006 |
| mouse anti-GAPDH | Santa Cruz Biotechnology | Cat#: sc-47724; RRID:AB_627678 |
| rabbit anti-GAPDH | Cell Signaling Technology | Cat#: 5174; RRID:AB_10622025 |
| mouse anti-α-tubulin | Santa Cruz Biotechnology | Cat#: sc-5286; RRID:AB_628411 |
| mouse anti-β-actin | Santa Cruz Biotechnology | Cat#: sc-47778 HRP; RRID:AB_2714189 |
| rabbit anti-pSer$^{795}$-Rb | Cell Signaling Technology | Cat#: 9301; RRID:AB_330013 |
| mouse anti-E2F-1 | Santa Cruz Biotechnology | Cat#: sc-56661; RRID:AB_783154 |
| rabbit anti-Cyclin D1 | Cell Signaling Technology | Cat#: 2978; RRID:AB_2259616 |
| rabbit anti-pSer$^{2}$-RPb1(CTD) | Cell Signaling Technology | Cat#: 13499; RRID:AB_2798238 |
| rabbit anti-H3K36me3 | Cell Signaling Technology | Cat#: 4909; RRID:AB_1950412 |
| mouse anti-GFP | DSHB | Cat#: DSHB-GFP-12E6; RRID:AB_2617418 |
| rabbit anti-ENL | Bethyl | Cat#: A302-267A; RRID:AB_1730821 |
| mouse anti-cyclin T1 | Santa Cruz Biotechnology | Cat#: sc-271575; RRID:AB_10650141 |
| control mouse IgG | Santa Cruz Biotechnology | Cat#: sc-2025; RRID:AB_737182 |
| control rabbit IgG | Santa Cruz Biotechnology | Cat#: sc-2027; RRID:AB_737197 |
| mouse anti-BrdU | Sigma-Aldrich | Cat#: B2531; RRID:AB_476793 |
| rabbit anti-Ki67 | Santa Cruz Biotechnology | Cat#: sc-15402; RRID:AB_2250495 |
| HRP-conjugated anti-rabbit | Cell Signaling Technology | Cat#: 7074; RRID:AB_2099233 |
| HRP-conjugated anti-mouse | Cell Signaling Technology | Cat#: 7076; RRID:AB_330924 |
| HRP-conjugated anti-rat | Cell Signaling Technology | Cat#: 7077; RRID:AB_10694715 |
| Alexa Fluor 488-conjugated goat anti-mouse IgG (H+L) | Molecular Probes (invitrogen) | Cat#: A-11029; RRID:AB_138404 |
| Alexa Fluor 488-conjugated goat anti-rabbit IgG (H+L) | Molecular Probes (invitrogen) | Cat#: A-11008; RRID:AB_143165 |
| **Bacterial and virus strains** | | |
| Stbl2 competent cells | Thermo Fisher | Cat#: 10268019 |
| Stbl3 competent cells | Thermo Fisher | Cat#: C737303 |
| DH5 alpha competent cells | Thermo Fisher | Cat#: 18258012 |
| XL10-Gold ultracompetent cells | Agilent | Cat#: 200314 |
| **Chemicals, peptides, and recombinant proteins** | | |
| Urea | Sigma-Aldrich | Cat#: U5128 |
| BrdU (5-bromo-2′-deoxyuridine) | Sigma-Aldrich | Cat#: B5002 |

(*Continued on next page*)

*Continued*

| REAGENT or RESOURCE | SOURCE | IDENTIFIER |
|---|---|---|
| Thymidine | Sigma-Aldrich | Cat#: T1895 |
| JQ1 | Selleckchem | Cat#: S7110 |
| Propidium Iodide | Invitrogen | Cat#: P3566 |
| Phenol/chloroform | Fisher Scientific | Cat#: PI17909 |
| para-formaldehyde | Sigma-Aldrich | Cat#: P6148 |
| Xylene | Fisher Scientific | Cat#: HC7001GAL |
| Hydrogen Peroxide | Fisher Scientific | Cat#: H325-500 |
| **Critical commercial assays** | | |
| NE-PER Nuclear and Cytoplasmic Extraction kit | Thermo Scientific | Cat#: PI78833 |
| DAB peroxidase substrate kit | Vector Laboratories | Cat#: SK-4105 |
| high capacity reverse transcription kit | ThermoFisher | Cat#: 4368814 |
| Mammary Life Medium complete kit | Lifeline Cell Technology, CA, | Cat#: LL-0061 |
| PowerUP SYBR Green Master Mix | Fisher Scientific | Cat#: A25743 |
| **Deposited data** | | |
| TCGA RNA-seq and outcome data | FireBrowse and UCSC Xena Browser | http://firebrowse.org/; https://xenabrowser.net/datapages/ |
| CPTAC proteomic and outcome data | CPTAC Data Portal | https://cptac-data-portal.georgetown.edu/ |
| GEO and EGA microarray and outcome | KM plotter | http://kmplot.com |
| RNA-seq data (MCF-7 cells) | This paper | GEO: GSE144372 |
| Combined TCGA and GTEx RNA-seq data | Wang et al., 2018 | https://figshare.com/articles/dataset/Data_record_3/5330593 |
| **Experimental models: cell lines** | | |
| MCF-10A | ATCC | CRL-10317 |
| HuMEC | ATCC | CRL-3243 |
| MDA-MB-231 | ATCC | HTB-26 |
| T47D | ATCC | HTB-133 |
| MCF-7 | ATCC | HTB-22 |
| BT549 | ATCC | HTB-122 |
| HEK293T | ATCC | CRL-11268 |
| CAMA-1 | ATCC | HTB-21 |
| HCC70 | ATCC | CRL-2315 |
| SK-UT-1 | ATCC | HTB-114 |
| SK-LMS-1 | ATCC | HTB-88 |
| **Experimental models: organisms/strains** | | |
| Female NU/NU Nude mouse | Charles River Laboratories | Strain code #088 |
| **Oligonucleotides** | | |
| Oligonucleotides for shRNA and sgRNA | See Table S5A | N/A |
| Primers for RT-qPCR and ChIP-qPCR | See Tables S5B and S5C | N/A |
| **Recombinant DNA** | | |
| PFN1(RNAi-Res #2) | This Paper | N/A |
| YFP | Diamond et al., 2015 | N/A |
| YFP-NLS-PFN1(WT) | Diamond et al., 2015 | N/A |
| YFP-NLS-PFN1(S137D) | Diamond et al., 2015 | N/A |
| YFP-NES-PFN1(WT) | Diamond et al., 2015 | N/A |
| YFP-PFN1(WT) | This Paper | N/A |
| XPO6(WT) | GeneCopoeia | Cat#: EX-W2830-Lv151 |

(*Continued on next page*)

*Continued*

| REAGENT or RESOURCE | SOURCE | IDENTIFIER |
|---|---|---|
| XPO6(RNAi-Res) | This Paper | N/A |
| PFN1(RNAi-Res #1) | This Paper | N/A |
| PFN1(WT) | This Paper | N/A |
| PFN1(S137D) | This Paper | N/A |
| Software and algorithms | | |
| GSEA software 4.0 | Subramanian et al., 2005 | N/A |
| Integrated Genome Viewer | Robinson et al., 2011 | https://igv.org/ |
| RStudio / ggplot2 | The R foundation | N/A |
| Cellsens software | Olympus Lifescience | N/A |
| ImageJ with Intensity Ratio Nuclei Cytoplasm Tool macros | ImageJ | Intensity_Ratio_Nuclei_Cytoplasm.ijm |
| Python 3.8 | Python Software Foundation | N/A |
| FlowJo 10 | FlowJo LLC | N/A |
| GraphPad Prism 7.0 | GraphPad software | N/A |
| Other | | |
| RIPA buffer | Cell Signaling Technology; EMD Millpore | Cat#: 9806; Cat#: 20-188 |
| Dynabeads Protein G | ThermoFisher | Cat#: 10004D |
| ChIP-Grade Protein G Agarose Beads | Cell Signaling Technology | Cat#: 9007 |
| GFP-Trap® Agarose Beads | Chromotek | Cat#: gta-20 |
| Target Retrieval Solution Citrate pH 6.0 | Dako | Cat#: S2369 |
| SuperSignal West Dura Extended Duration Substrate | ThermoFisher | Cat#: 34075 |
| West Femto Maximum Sensitivity Substrate | ThermoFisher | Cat#: 34096 |

## RESOURCE AVAILABILITY

### Lead contact

Further information and requests for resources and reagents should be directed to and will be fulfilled by the Lead Contact, Jieya Shao (shao.j@wustl.edu)

### Materials availability

Reagents generated in this study will be made available on request with a completed Materials Transfer Agreement.

### Data and code availability

RNA-seq data generated in this study are available at the GEO data depository under accession number GSE144372. No unique code was generated.

## EXPERIMENTAL MODEL AND SUBJECT DETAILS

### Cell lines

All cell lines except for mouse chondrocytes were purchased from ATCC and authenticated and tested for mycoplasma. MCF-10A cells were grown in DMEM/F12 plus 5% or 10% horse serum and supplements (50 μg/mL gentamycin, 20 ng/mL EGF, 0.5 mg/mL hydrocortisone, 100 ng/mL cholera toxin, and 10 μg/mL insulin). HuMEC cells were cultured using the MammaryLife Medium complete kit (Lifeline Cell Technology, CA, cat #LL-0061). MCF-7 and T47D cells were grown in RPMI 1640 plus 5% or 10% fetal bovine serum (FBS) and supplements (50 μg/mL gentamycin, 1mM sodium pyruvate, 10 mM HEPES and glucose to 4.5 g/L). MDA-MB-231, BT-549, CAMA-1, HCC70, HEK293T, and mouse chondrocytes were grown in high glucose DMEM plus 5% or 10% fetal bovine serum and 50 μg/mL gentamicin. SK-UT-1 and SK-LM-1 were grown in MEM plus 10% fetal bovine serum and 50 μg/mL gentamicin.

### Animal experiments

All animal experiments were performed in accordance with the guidelines recommended by the National Institutes of Health. 4-week old female *NU/NU* nude mice were purchased from Charles River and kept for one week under standard institutional care. For ER-positive MCF-7 cells, estrogen pellets (17β estradiol, 0.75 mg/pellet, 90 days release; Innovative Research of America, Sarasota, FL)

were implanted subcutaneously a day before tumor cell implantation. MCF-7 cells stably expressing XPO6(WT) and XPO6 (RNAi-Res) and infected with shLUC or shXPO6#3, were trypsinized, washed with and re-suspended in Hank's balanced salt solution (HBSS), and mixed at a 1:1 ratio with Matrigel (356237, BD Biosciences). 5 × $10^6$ (in 75 μl) cells were injected bilaterally into the 4$^{th}$ mammary glands of each mouse (6 mice/group). For ER- MDA-MB-231 cells stably infected with lentiCRISPRv2.0 lacking (control) or containing sgXPO6 #1 or #3, 1.7 × $10^6$ in 75 μl were injected bilaterally into the 4$^{th}$ mammary fad pads of female nude mice without estrogen pellets (10 mice per group). Tumor volumes were measured bi-weekly by Caliper. Tumor volumes were calculated using the formula: tumor volume [$mm^3$] = 1/2 x (tumor length) x (tumor width)$^2$ . For MCF-7 cells, the experiment was terminated at 11 weeks post injection when the largest tumors reached around 1.5cm in diameter. For MDA-MB-231 cells, mice in each group were randomly divided into vehicle and JQ1 treatment groups (3-5 mice per group depending on the numbers of tumor-bearing mice) when the average tumor volume reached approximately 70$mm^3$. JQ1 (S7110, Selleckchem) was freshly prepared each day by diluting 10x stock solution (0.5 mg/6 μl, 83.3mg/ml, in DMSO) into 1x working solution (0.05 mg/6 μl) using vehicle (10% hydroxypropyl beta cyclodextrin in 0.9% sodium chloride). Mice received intraperitoneal injection of equal volume of vehicle or JQ1 at a daily dose of 50mg/kg for three weeks, during which tumors were measured semiweekly. Mice were euthanized and tumors were resected, weighed, and saved for further analyses.

## METHOD DETAILS

### Antibodies

Primary antibodies used for western blot are as follows: rabbit anti-XPO6 (Thermo Fisher, #PA5-31813), mouse anti-RPb1(CTD) (Cell Signaling, #2629), rabbit anti-Cdk9 (Cell Signaling, #2316), rabbit anti-cyclin T1 (Cell Signaling, #81464), rabbit anti-GFP (Cell Signaling, #2956), rabbit anti-Histone H3 (Cell signaling, #4499), rabbit anti-Pfn1 (Cell signaling, #3237; Abcam, ab124904, Sigma, P7624), rat anti-GFP (Biolegend, 338002), rabbit anti-ENL (Bethyl lab, A302-268A), mouse anti-GAPDH (Santa cruz, sc-47724), rabbit anti-GAPDH (Cell Signaling, # 5174), mouse anti-α-tubulin (Santa Cruz, sc-5286). mouse anti-β-actin (Santa Cruz, sc-47778), rabbit anti-p-Rb(Ser$^{795}$) (Cell Signaling, #9301), mouse anti-E2F-1 (Santa Cruz, sc-56661), rabbit anti-Cyclin D1 (Cell Signaling, #2978) antibodies. Primary antibodies for ChIP include rabbit anti- p-Rpb1(Ser$^2$) (CTD) (Cell Signaling, #13499), rabbit anti-Cdk9 (Cell Signaling, #2316), rabbit anti-cyclin T1 (Cell Signaling, #81464), rabbit anti-ENL (Bethyl lab, A302-268A), rabbit anti-H3K36me3 (Cell Signaling, #4909) antibodies. Primary antibodies used for immunoprecipitation are as follows: mouse anti-GFP (DSHB, #12E6), GFP-Trap agarose (Chromotek, Cat # gta-20), rabbit anti-ENL (Bethyl lab, A302-267A), mouse anti-cyclin T1 (Santa Cruz, sc-271575), control IgG (Santa Cruz, sc-2027 and sc-2025). Mouse anti-BrdU antibody for immunofluorescence staining (B2531) was purchased from Sigma. Primary antibodies for immunofluorescence staining include rabbit anti-Pfn1 (Abcam, ab124904). Antibodies for immunohistochemistry include rabbit anti-Ki67 (Santa Cruz, sc-15402), rabbit anti-p-Rb(Ser$^{795}$) (Cell Signaling, #9301) antibodies. Secondary antibodies for western blots are horseradish peroxidase-conjugated anti-rabbit (Cell Signaling, #7074), anti-mouse (Cell Signaling, #7076), and anti-rat (Cell Signaling, #7077) antibodies. Secondary antibodies for immunofluorescence are Alexa Fluor 488-conjugated goat anti-mouse or rabbit IgG (H+L) (Invitrogen, A-11029 and A-11008). Secondary antibodies for immunohistochemistry are SignalStain Boost IHC Detection Reagents (Cell Signaling, #8114 and #8125).

### Plasmids, shRNAs, and sgRNAs

Three shRNAs targeting human XPO6, a shRNA targeting luciferase (Zhu et al., 2020), and a shRNA targeting human ENL in the lentiviral pLKO.1 vector were purchased from Sigma. *XPO6* cDNA in the lentiviral vector pEZ-Lv151 was purchased from GeneCopoeia (# EX-W2830-Lv151). Silent mutations resistant to shXPO6 #3 (GGAAAGGTTGGTC to AGAGCGCCTCGTG) were introduced by Genewiz between nucleotides 1861-1877 in the *XPO6* cDNA (numbering after ATG). Two shRNAs targeting human Pfn1 and a scrambled shCTRL were cloned in the lentiviral pFLRu-FH vector (Diamond et al., 2015). Silent mutations resistant to shPFN1 #1 and #2 were introduced in human *Pfn1* cDNA by QuickChange: AGC to TCG (nucleotide 253-255) and TTG to CTC (nucleotide 367-369). Paired guide RNAs specific for human *XPO6* gene used with Cas9 (D10A) nickase (Cas9n) were designed using E-CRISP (http://www.e-crisp.org/E-CRISP/). Oligonucleotides for four pairs of sgRNAs were synthesized, each pair consisting of two annealed oligonucleotides whose target sequences in *XPO6* are ≤ 20 base pairs apart. Following oligo annealing, they were inserted into the BbsI sites of the pSpCas9n(BB)-2A-Puro vector (PX462, Addgene 48141) (Ran et al., 2013). Single guide RNAs for human *XPO6* used with wild-type Cas9 were similarly designed, and cloned into the BsmBI site in the lentiCRISPRv2.0 vector (Addgene #52961).

### CRISPR/Cas9 editing

For gene editing with the Cas9(D10A) nickase, MDA-MB-231 cells were transfected at 80%–90% confluence in 24-well plates with 1.0μg pSpCas9n(BB)-2A-Puro (expressing Cas9n) alone or individual pairs of XPO6-targeting gRNAs (#1-4) in the same vector (0.5/0.5μg) with 3μl lipofectamine 2000. Transfected cells were treated with 1μg/ml puromycin for 3-4 days till the untransfected cells died off. To obtain single clones, pooled cells were diluted to less than 1 cell per 100μl, and 100μl were plated in each well in a 96-well plate to minimize the likelihood of having > 1 cell per well. Visually confirmed single cells were expanded, confirmed for XPO6 loss, and used for further experiments. For gene editing with wild-type Cas9, MDA-MB-231 and MCF-7 cells were infected with lentiviral particles consisting of empty lentiCRISPRv2 or the same vector with individual XPO6-targeting sgRNAs. Viral production has been described previously (Diamond et al., 2015).

### *In vitro* growth assays

Proliferation assays were performed by seeding approximately 500 cells/well in 96-well plates, followed by quantification by Alamar blue assay on a fluorescence plate reader on day 1 and subsequent time points as indicated in the specific experiments. Relative effects of shXPO6 knockdown were expressed as % decrease in the growth rates (day n/day 1) of shXPO6-infeceted cells relative to shLUC-infected cells. Colony formation assays were performed by seeding approximately 500 cells/well in 6-well plates (or proportionally in 12-well or 24-well plates) and cultured for 9-12 days in the absence or presence of different drugs. Cells were quantified by Alamar blue prior to fixation with 4% paraformaldehyde for 15min and staining with 0.005% crystal violet for 2h. Colonies were imaged and quantified for percentages of occupied areas in the wells by ImageJ.

### Cell cycle analysis

Standard double thymidine block (2mM thymidine, 18hr first block, 9hr release, 16hr second block) and DNA content analysis by propidium iodide staining and flow cytometry were conducted. Cell cycle analysis was performed using the univariate Watson model of FlowJo.

### Co-immunoprecipitation and mass spectrometry

Nuclear lysates of approximately 20 × $10^6$ MDA-MB-231 cells were prepared using the NE-PER Nuclear and Cytoplasmic Extraction kit (Thermo Scientific, PI78833) according to the manufacturer's protocol. Nuclear lysates were diluted 2x with 10mM Tris-HCl, pH 7.4 in 0.5% Triton X-100, 1x protease (#A32955, ThermoFisher) and phosphatase (#A32957, ThermoFisher) inhibitors, quantified by the Bradford assay, and equal amounts were mixed with ~50μl GFP-Trap agarose beads (Cat # gta-20, Chromotek) to capture YFP and YFP-tagged NLS-Pfn1(WT versus S137D). After binding at 4°C for 4 hr, beads were washed four times with 10mM Tris-HCl, pH 7.4, 150mM NaCl, 0.5% Triton X-100. Proteins were eluted by SDS sample buffer and subjected to filter-aided sample preparation (FASP) (Erde et al., 2014; Wiśniewski et al., 2009) and trypsin digestion. Briefly, 30 μl samples were mixed with 200 μl UA buffer consisting of 8M urea (Sigma, U5128) in 0.1M Tris-HCl, pH 8.5, and added to Microcon YM-30 filter units (Millipore, MRCF0R030). Samples were spun for 15 min at 14,000 x g and washed twice with 100 μl UA buffer by centrifugation at the same speed for the same length of time. 100 μL of 50 mM iodoacetamide (freshly dissolved in UA buffer) were added, incubated for 20 min at 20°C in the dark. Samples were centrifuged at 14,000 x g for 10 min, washed twice with 100 μl UA buffer, and 60 μL of sequencing-grade trypsin (Sigma, #11418025001) (200-400 ng total) in 50mM ammonium bicarbonate was added to the filter units. Following overnight digestion at 37°C, samples were collected by centrifugation at 14,000 x g for 10 min. 50 μl of 0.5M NaCl was added to the filters, centrifuged at 14,000 x g for 10 min. Pooled eluates were acidified to 5% formic acid (FA), cleaned up by C18 zip-tips (# ZTC18S096, Millipore, and resuspended in 15 μl 1% formic acid/1% acetonitrile.

Samples were analyzed by reverse-phase liquid chromatography-electrospray ionization-MS/MS using an Eksigent cHiPLC Nanoflex microchip system connected to a quadrupole time-of-flight TripleTOF 5600 mass spectrometer (ABSCIEX). The Nanoflex system uses replaceable microfluidic traps and columns packed with ChromXP C18 (200um ID x 15cm, 3 μm particle, 120 Å) for online trapping, desalting, and analytical separations. Solvents composed of water/acetonitrile/formic acid (A, 100/0/0.1%; B, 0/100/0.1%). A 200 ng to 1μg portion of sample was loaded (typically, 2-10 μl of sample was injected) into column with 98% mobile phase A. After online trapping, peptide mixtures were eluted into analytical column at a flow rate of 800 nL/min using the following gradient: (1) starting at 2% solvent B; (2) 2%–5% solvent B from 0 to 12 min; (3) 5%–22% solvent B from 12 to 120 min; (4) 22%–30% solvent B from 120 to 150 min; (5) 30%–80% solvent from 150 to 165 min; and finally 80%(vol/vol) solvent from 165 to 169 min with a total run time of 180 min including mobile phase equilibration. The LC column was maintained at 35°C during the run. For Data dependent acquisitions, mass spectra and tandem mass spectra were recorded in positive-ion and high-sensitivity mode. The nanospray needle voltage was typically 3,800 V. After acquisition of each sample, TOF MS spectra and TOF MS/MS spectra were automatically calibrated during dynamic LC-MS and MS/MS auto calibration acquisitions by injecting 50 fmol β-galactosidase. For collision-induced dissociation tandem MS (CID-MS/MS), the mass window for precursor ion selection of the quadrupole mass analyzer was set to ± 1 *m/z*. The precursor ions were fragmented in a collision cell using nitrogen as the collision gas. Advanced information-dependent acquisition (IDA) was used for MS/MS collection on the TripleTOF 5600 to obtain MS/MS spectra for the 20 most abundant parent ions following each survey MS1 scan (allowing typically for 80 ms acquisition time per each MS/MS). Dynamic exclusion features were set to an exclusion mass width of 50 mDa and an exclusion duration of 30 s.

Protein identification and MS1 quantification was performed with MaxQuant (Cox and Mann, 2008) against the UniProt Human Reference Proteome. The MS/MS spectra were searched with fixed modification of Carbamidomethyl-Cysteine, variable modifications of oxidation (M), acetylation (protein N-term). Search parameters were set to an initial precursor ion tolerance of 0.07 Da, MS/MS tolerance at 40 ppm and requiring strict tryptic specificity with a maximum of two missed cleavages. The minimum required peptide length was set to seven amino acids. Peptide identification FDR was set at 1%.

### Co-immunoprecipitation and western blot

For MCF-7 cells expressing YFP and NLS-YFP-Pfn1(WT and S137D), nuclear extracts were prepared using a modified Stillman protocol (Méndez and Stillman, 2000). Briefly, approximately 5 × $10^6$ cells were lysed with 200 μl hypotonic buffer A (10 mM HEPES, pH 7.9, 10 mM KCl, 1.5 mM MgCl2, 0.34 M Sucrose, 10% Glycerol, 1 mM DTT, 0.1% Triton X-100, Protease and phosphatase inhibitor cocktails) for 15min on ice, and centrifuged at 1,300 g for 5 min. After removing cytosol, nuclei were washed once with buffer A

without Triton X-100, and lysed with 200 μl nuclear buffer (10mM HEPES, pH 7.0, 200mM NaCl, 1mM EDTA, 0.5% NP-40, and protease-inhibitor cocktail) for 10 min on ice followed by centrifugation at 13,000 g for 10 min. Clarified nuclear lysates were incubated with 2 μg of the GFP antibody (DSHB, #12E6) overnight at 4°C with rotation and mixed with 30 μL of the protein G beads (CST, #9007S) at 4°C for 1-2 hr. The beads were then washed 3-5 times with IP buffer (40 mM Tris-Cl, pH 7.5, 150 mM NaCl, 2mM EDTA, 0.5% Triton X-100, 10% glycerol, and 1 mM DTT), and heated at 95°C in SDS sample buffer for 5 min. For parental and shLUC or shENL-infected MCF-7 cells, approximately 5 × $10^6$ cells were lysed with 800ul RIPA buffer (EMD Millpore, 20-188) and centrifuged at > 15,000 g for 10 min. 350ul of clarified lysates were incubated for 3 hr at 4°C with 20 μL of protein G magnetic Dynabeads (Thermo Fisher, 10004D), and 3 μg of normal IgG, ENL, or Cyclin T1 antibodies. Beads were washed 6 times with cold PBS + 0.02% Tween-20, followed by heating in SDS sample buffer. All samples were subsequently analyzed by SDS-PAGE and western blot analysis.

For analyzing proteins in cell lysates by western blot, lysates were prepared using RIPA buffer (CST, #9806) supplemented with protease and phosphatase inhibitors and clarified by centrifugation at 15,000 g for 10min. After normalization using the Quick Start Bradford 1x Dye Reagent (Bio-Rad, #5000205), 1-10 μg denatured proteins were analyzed by SDS-PAGE and transferred to nitrocellulose membrane (Santa Cruz, sc-3718). Primary antibodies were incubated overnight at 4°C in TBS/0.1% Tween-20 containing 5% bovine serum albumin. Secondary antibodies were incubated at room temperature for 1-2 hr. Proteins were developed using the SuperSignal West Dura Extended Duration Substrate (34075, ThermoFisher) or West Femto Maximum Sensitivity Substrate (34096, ThermoFisher), and imaged on a Gel Doc XR imaging system (Bio-Rad). Band intensities were quantified by ImageLab.

### Size exclusion chromatography

Nuclei from 15-20 × $10^6$ MDA-MB-231 cells were prepared as described above (under immunoprecipitation and western blot) using a modified Stillman protocol, and lysed in RIPA buffer. Following sonication and clarification, nuclear extracts were applied to a RIPA-equilibrated ENRICH 650 gel filtration column (Bio-Rad) for size exclusion separation. RIPA buffer was used to elute the proteins with a flow rate of 0.5 mL per minute. Fractions were collected, denatured in SDS sample buffer, and analyzed by western blot.

### BrdU labeling

MCF-7 and MDA-MB-231 cells were incubated with growth media containing 10 μM BrdU for 1 hr and 30 min respectively at 37°C in the $CO_2$ incubator. Cells were permeabilized by PBS/0.1% Triton X-100, denatured by 2M HCl for 30 min and neutralized by 0.1M sodium tetraborate for 2 min. Primary anti-Brdu antibody (1:200) and Alexa 488-conjugated secondary anti-mouse IgG (1:1000) were used for the immunofluorescence staining. Propidium Iodide (PI) (20 μg/ml) was used for nuclear staining.

### Immunofluorescence staining, cell imaging, and nuclear/cytoplasmic intensity analysis

1x $10^4$ MCF-7 and MDA-MB-231 cells were seeded in 96-well plates, fixed with 4% para-formaldehyde for 15min, washed with PBS, permeabilized by PBS/0.1% Triton X-100 for 10 min, blocked for 30 min in 2% BSA/2% normal goat serum in PBS/0.1% Tween-20, and incubated with rabbit anti-Pfn1 antibody (1:1000) in the blocking buffer overnight at 4°C. Cells were washed three times with PBS/0.1% Tween-20, incubated with Alexa 488-conjugated goat anti-rabbit secondary antibody (Invitrogen #A-11008, 1:1000) and DAPI for 1hr at room temperature, and washed three times with PBS.

Cell lines expressing YFP-Pfn1 or YFP-actin were grown in 96-well plates, fixed for 15min by 4% para-formaldehyde, washed and permeabilized as above, counterstained with DAPI, followed by PBS wash.

Imaging was done on an inverted epifluorescence microscope (Olympus IX70) using a 20x objective and CellSens as the acquisition software. High resolution images were captured by choosing the pixel shift function of the camera at the highest setting (4140 × 3096). ImageJ was used for merging and quantifying nuclear and cytoplasmic fluorescence by the Intensity Ratio Nuclei Cytoplasm Tool macros. 500-1000 cells were analyzed per experiment.

### Immunohistochemistry

5 μm formalin-fixed and paraffin-embedded tumor tissues were subjected to standard IHC protocols. Briefly, tissues were rehydrated through serial washes with xylene and ethanol (100%, 95%, 80%, and 70%). Antigen was retrieved by heating tissues in Target Retrieval Solution Citrate pH 6.0 (Dako, #S2369) for 20 min followed by quenching with 3mM hydrogen peroxide for 10 min. After washing with TBST (TBS/0.1% Tween-20) and blocking with 5% normal goat serum in TBST for 1 hr at room temperature, tissues were incubated with primary antibodies (Ki67, 1:500; p-Rb($Ser^{795}$), 1:500) in blocking buffer at 4°C overnight, washed with TBST, incubated with HRP-conjugated secondary antibodies for 2 hr at room temperature, washed with TBST, and developed using the DAB peroxidase substrate kit (Vector Laboratories, #SK-4105).

### qRT-PCR

Total RNAs of cells grown in 12-well or 6-well plates were isolated using 250 or 500 μl TRIzol (Invitrogen) according to manufacturer's instruction. Total RNAs from tumor samples stored in RNAlater solution was isolated the same way. Residual DNA was digested with RNase-free DNase I (1 μg RNA /1 U enzyme) (ThermoFisher) for 37°C for 30 min. Complementary DNAs were synthesized from 2 μg RNA using the high capacity reverse transcription kit (4368814, ThermoFisher), and quantitative PCR was performed using the PowerUP SYBR Green Master Mix (A25743, Fisher Scientific) in accordance with the manufacturer's instruction

on a CFX96 Touch Real-Time PCR Detection System (Bio-Rad). Relative mRNA levels for each gene of interest were obtained by normalizing to GAPDH mRNA levels using the comparative cycle threshold (Ct) method. Primers were designed using Primer-Blast at NCBI or based on published papers (Erb et al., 2017; Kim et al., 2013; McLaughlin-Drubin et al., 2011; Rengasamy et al., 2017; Struntz et al., 2019).

### ChIP-qPCR

1-2 x$10^7$ cells were cross-linked with 1% formaldehyde for 10 min, quenched with 125mM glycine for 5 min, washed twice with cold PBS, and collected by scraping and centrifugation at 1,000 g for 5 min. Cells were resuspended in 750 μl lysis buffer (50mM Tris-HCl, pH 8.0, 10mM EDTA, 1% SDS, protease inhibitors), and sonicated using a Bioruptor Sonicator (Diagenode). Samples were centrifuged at 12,000 rpm for 10 min at 4°C, and supernatants containing ~25 μg total DNA were diluted 10 times with IP buffer (16.7 mM Tris-HCl pH 8.0, 167 mM NaCl, 1.2 mM EDTA, 0.01% SDS, 1.1% Triton X-100) and mixed with 2-4 μg antibodies overnight at 4°C. 20-60 μl protein G-conjugated dynabeads (10003D, Thermo Fisher) were added and incubated for 2 hr at 4°C, washed three times with 20mM Tris-HCl pH 8.0, 150 mM NaCl, 2mM EDTA, 1% Triton X-100, 0.1% SDS, followed by one final wash with the same buffer with 500mM NaCl. DNAs were eluted from beads twice with 200 μl elution buffer (100mM NaHCO3, 1% SDS) each time for 15 min at room temperature, and the eluates were combined. NaCl was added to the DNAs at a final concentration of 0.3M, and samples were incubated at 65°C overnight to de-crosslink. 20 mg/ml proteinase K was added and incubated at 45°C for 2 hr. DNAs were extracted by phenol/chloroform (PI17909, Fisher Scientific), washed with 70% ethanol, dried, and resuspended in ~40 μl water. Quantitative PCR was performed as described for qRT-PCR. The comparative cycle threshold (Ct) method was used to determine enrichment relative to the level of input DNA (2%) or non-specific IgG control.

### RNA-seq

RNA was extracted from ~2 × $10^6$ MCF-7 cells using the RNeasy Mini Kit as per the manufacturer's protocol (QIAGEN). Two biological replicates were included for each experimental condition. Sample quality was assessed using Agilent BioAnalyzer. Samples were prepared according to library kit manufacturer's protocol, indexed, pooled, and sequenced on an Illumina NovaSeq.

## QUANTIFICATION AND STATISTICAL ANALYSIS

### TCGA gene expression analyses

TCGA RNA-seq data (rnaseqv2_unc_edu_Level_3_RSEM_genes_normalized_data for all cancer types) were downloaded from FireBrowse. These gene-level data had been previously quantified and normalized by TCGA with the RNASeqV2 pipeline using RNA-Seq by Expectation Maximization (RSEM) (Li and Dewey, 2011). Data were analyzed by Python 3.8 for statistical significance with the Scipy, Pingouin, and Scikit Posthocs packages. Graphs were generated by GraphPad Prism 7.0. For Figures 1A and S6A and Tables S1A, S1B, and S1D, Mann-Whitney U non-parametric tests were used to calculate the statistical significance of the difference in XPO6 and Pfn1 mRNA levels between unmatched tumor and normal tissue samples. For Figures 1B and S6B and Table S1C, Wilcoxon Signed Rank non-parametric tests were used to calculate the statistical significance of the difference in XPO6 and Pfn1 mRNA levels between paired tumor and adjacent normal samples. For Figure S1A, a non-parametric one-way ANOVA (Kruskal-Wallis) with Dunn's multiple comparison test was performed to analyze the difference in XPO6 mRNA levels among breast cancer PAM50 subtypes and normal tissues. For Figure 6G and Table S3, correlations between MYC mRNA level and those of XPO6, BRD4, and NCL in the various TCGA datasets were analyzed using Spearman's rank correlation coefficient. For hypothesis testing involving multiple comparisons, false discovery rate was controlled by using the Benjamini-Hochberg method. P and q values less than 0.05 were considered significant.

### Combined TCGA/GTEx gene expression analyses

Normalized, batch effect-corrected RNA-seq data from a study combining TCGA and GTEx datasets were retrieved from Figshare (https://figshare.com/articles/dataset/Data_record_3/5330593). For each of the 17 cancer types in Table S1B, RNA expression from TCGA tumor samples was compared to expression from a combined set of TCGA adjacent healthy samples and tissue-matching GTEx normal samples using Mann-Whitney U non-parametric tests. The Benjamini-Hochberg method was used to adjust p values. Data processing and hypothesis testing were performed using Python.

### CPTAC proteomic data analysis

For Figures S1D and S6D, processed mass spectrometry data of 125 tumors and 18 normal samples in the Clinical Proteomic Tumor Analysis Consortium (CPTAC) Breast Cancer Confirmatory Study were downloaded from the CPTAC Data Portal (https://cptac-data-portal.georgetown.edu/). Raw data had been processed through the CPTAC Common Data Analysis Pipeline (CDAP) and provided as log2 transformed normalized values against a common pool of reference samples. Statistical significance of the difference in protein abundance between tumor and normal samples were calculated using the Mann-Whitney U or Wilcoxon Signed Rank non-parametric tests for unpaired or paired samples by GraphPad Prism 7.0. P values less than 0.05 were considered significant.

### Kaplan-Meier survival analyses

Kaplan-Meier survival outcome analysis was performed using KM plotter (http://kmplot.com). For overall survival analysis of various TCGA datasets as undivided cohorts (Figures 1E and S6E) or stage-defined sub-cohorts (Figures 1F, 2A, and S6E), RNA-seq data and clinical information hosted by KM plotter were used. For overall and progression-free survival analysis of TCGA breast cancer patients divided based on lymph node and ER status (Figures S2B–S2D and S6F), RNA-seq data were downloaded from FireBrowse and curated clinical data (Liu et al., 2018) were downloaded from the UCSC Xena Browser, and then imported into KM plotter for statistical analysis and graph generation using the web-based custom plotting function. For relapse-free survival of breast cancer patients in the GEO and EGA datasets (Figures S2E–S2H, S6G, and S6H), gene chip data and clinical information hosted at KM plotter were used. For overall survival analysis against proteomic data (Figures 1G and S6I), a published study (Tang et al., 2018) consisting of mass spectrometry data and clinical information of 65 breast cancer patients available at KM plotter was used. For all analyses, median cutoff was chosen to split cohorts evenly into subgroups with high versus low mRNA or protein levels of XPO6 and Pfn1. For analyses using gene chip data, JetSet best probe sets for XPO6 and Pfn1 (Affimetrix ID 211982 and 200634) were selected. Log-rank tests were used to calculate p values.

### RNA-seq analysis

Basecalls and demultiplexing were performed with Illumina's bcl2fastq software and a custom python demultiplexing program with a maximum of one mismatch in the indexing read. RNA-seq reads were aligned to the Ensembl release 76 primary assembly with STAR version 2.5.1a. Gene counts were derived from the number of uniquely aligned unambiguous reads by Subread:featureCount version 1.4.6-p5. All gene counts were imported into the R/Bioconductor package EdgeR and TMM normalization size factors were calculated to adjust for samples for differences in library size. Ribosomal genes and genes not expressed in the smallest group size minus one sample greater than one count-per-million were excluded from further analysis. The TMM size factors and the matrix of counts were imported into the R/Bioconductor package Limma. Weighted likelihoods based on the observed mean-variance relationship of every gene and sample were then calculated for all samples with the voomWithQualityWeights. Differential expression analysis was then performed to analyze for differences between shXPO6 and shLUC-infected cells expressing XPO6(WT) or XPO6(RNAi-Res), and the results were filtered for only those genes with Benjamini-Hochberg false-discovery rate adjusted p values less than or equal to 0.05. For each contrast extracted with Limma, global perturbations in known Gene Ontology (GO) terms, MSigDb, and KEGG pathways were detected using the R/Bioconductor package GAGE to test for changes in expression of the reported log 2 fold-changes reported by Limma in each term versus the background log 2 fold-changes of all genes found outside the respective term. A subset of significantly enriched gene sets were plotted using R/ggplot2. Gene set enrichment analysis (GSEA) was performed using the GSEA software (4.0) (Subramanian et al., 2005). To visualize RNA-seq tracks for representative genes, 2-3 significantly downregulated genes in XPO6 knockdown cells expressing XPO6(WT) but not XPO6(RNAi-res) cells were chosen from each gene set. RNA-seq BAM files were converted to the BigWig format using DeepTools and sequencing data were normalized using the Reads Per Kilobase per Million mapped reads (RPKM) method. These normalized data were loaded into the Integrated Genome Viewer (Robinson et al., 2011) and replicates for each sample were summed together.

**Cell Reports, Volume *34***

## Supplemental Information

# Cancer-associated exportin-6 upregulation inhibits the transcriptionally repressive and anticancer effects of nuclear profilin-1

**Cuige Zhu, Sun-Joong Kim, Arshag Mooradian, Faliang Wang, Ziqian Li, Sean Holohan, Patrick L. Collins, Keren Wang, Zhanfang Guo, Jeremy Hoog, Cynthia X. Ma, Eugene M. Oltz, Jason M. Held, and Jieya Shao**

**Supplementary Figures**

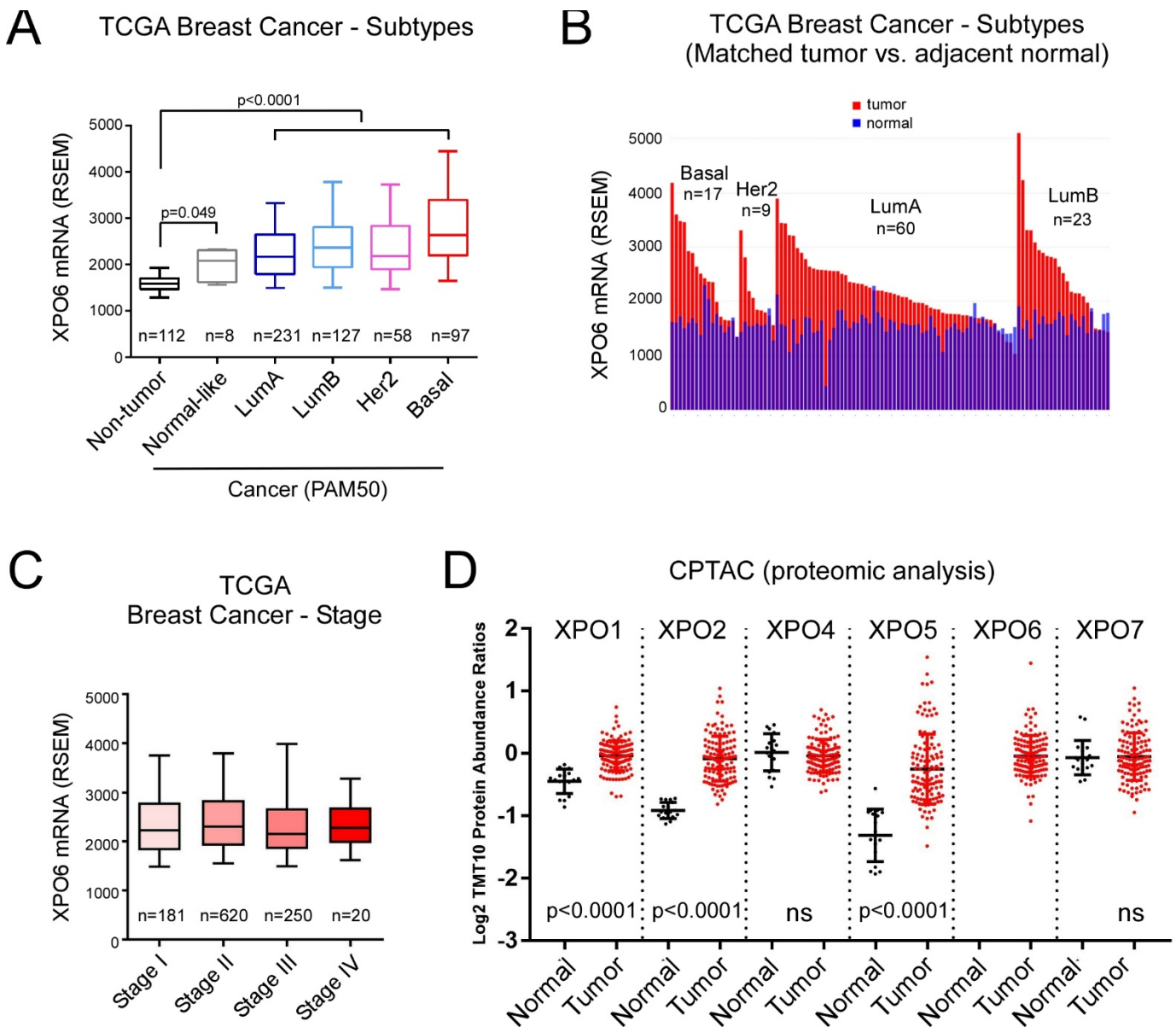


**Fig.S1 XPO6 upregulation in breast cancer, related to Figure 1.**
(A) *XPO6* mRNA levels in TCGA breast tumor samples divided into distinct molecular subtypes based on PAM50 classification. Non-tumor controls are adjacent healthy tissue samples. Whiskers extent to the 5-95 percentiles. P values were based on non-parametric one-way ANOVA (Kruskal-Wallis) with Dunn's post-hoc test. (B) *XPO6* mRNA levels in matched tumor and adjacent normal tissues of 112 breast cancer patients in the TCGA dataset divided into distinct molecular subtypes based on PAM50 classification. (C) *XPO6* mRNA levels in TCGA breast tumor samples divided based on stages. Whiskers extend to the 5-95 percentiles. (D) Protein levels of selected nuclear exportins (including XPO6) in 125 breast tumor and 18 normal breast tissue samples in the CPTAC confirmatory cohort detected by quantitative mass spectrometry analysis. P values were based on the Mann-Whitney U non-parametric test. Note: XPO6 was undetectable in normal breast tissues.

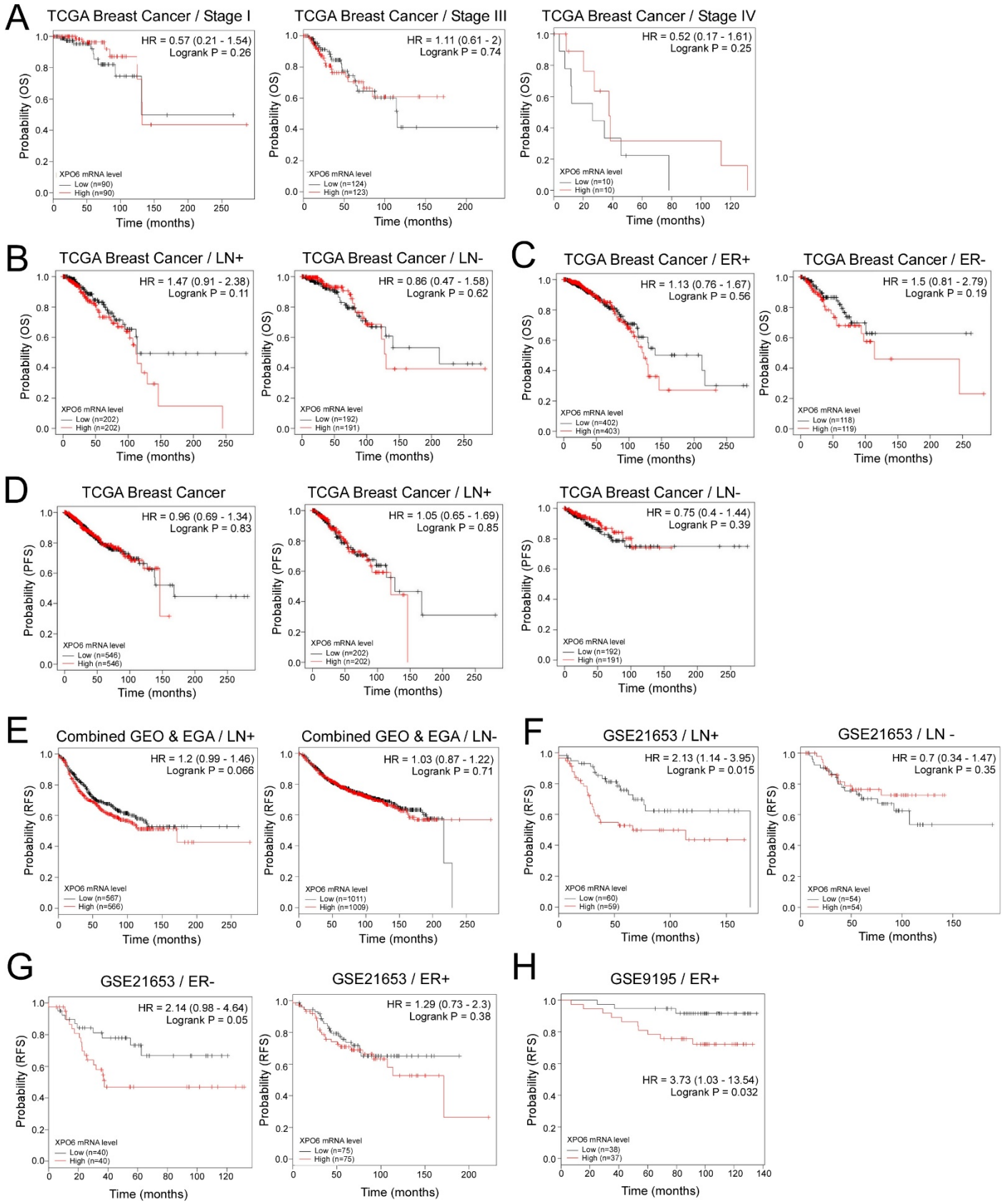


**Fig.S2 Association of *XPO6* mRNA level with breast cancer survival, related to Figure 1.**
(A) Univariate Kaplan-Meier analysis of the association between *XPO6* mRNA level and overall survival (OS) of TCGA breast cancer patients separated by stages. (B-C) Univariate Kaplan-Meier analysis of the association between *XPO6* mRNA level and OS of TCGA breast cancer patients separated by the status of lymph node

spread (B) and ER positivity (C). (D) Univariate Kaplan-Meier analysis of the association between *XPO6* mRNA level and progression-free survival (PFS) of TCGA breast cancer patients as a while cohort or separated by lymph node status. (E) Univariate Kaplan-Meier analysis of the association between *XPO6* mRNA level and relapse-free survival (RFS) of breast cancer patients in the combined GEO and EGA datasets (35 in total) separated by lymph node status. (F-G) Univariate Kaplan-Meier analysis of the association between *XPO6* mRNA level and RFS of breast cancer patients in the GSE21653 dataset consisting of 227 early-stage breast cancer patients separated by lymph node status (F) or ER positivity (G). (H) Univariate Kaplan-Meier analysis of the association between *XPO6* mRNA level and RFS of ER-positive, tamoxifen-treated, early-stage breast cancer patients (n=75) in the GSE9195 (also known as GUYT2) dataset (Loi et al., 2008). All the analyses were performed using KM plotter with median cutoff to evenly divide patient cohorts into high and low *XPO6* subgroups. For GEO/EGA datasets, JetSet best probe set for human XPO6 gene (211982) was selected. P values were based on the log-rank test.

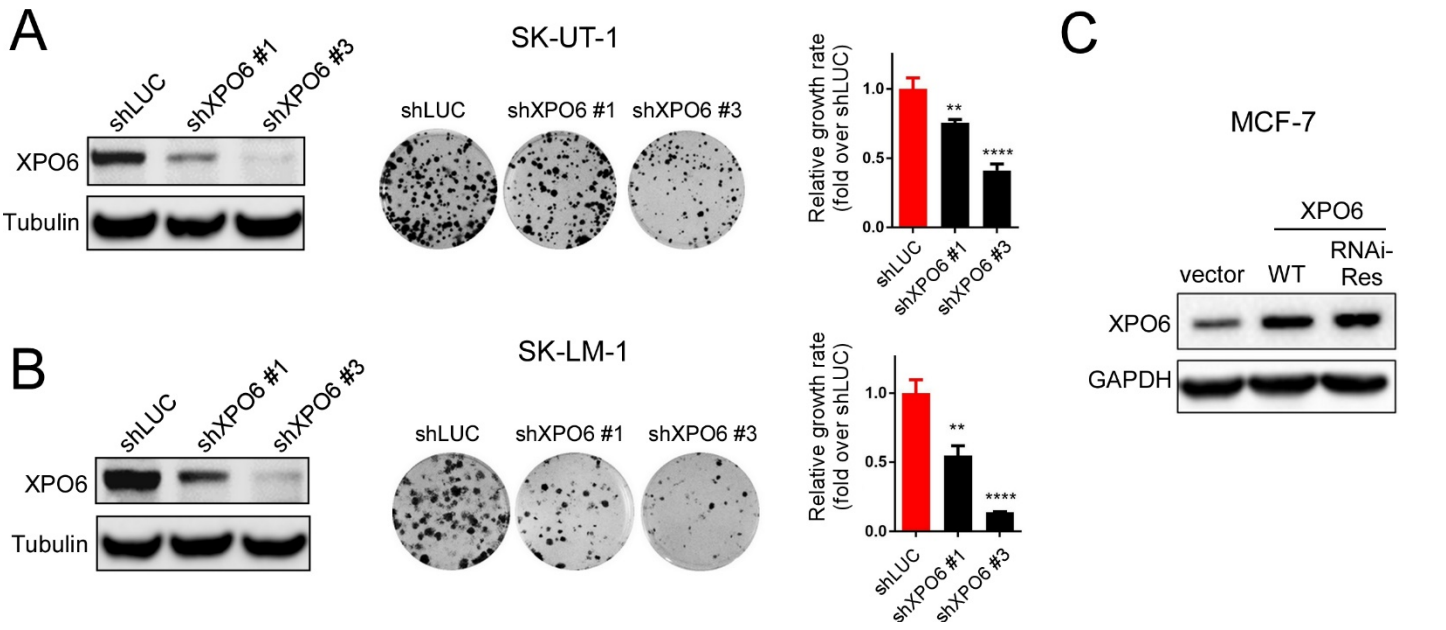


**Fig.S3 Effect of XPO6 knockdown on the growth of soft tissue sarcoma cell lines, related to Figure 2.** (A-B) Soft tissue sarcoma cell lines SK-UT-1 and SK-LM-1 were infected with shLUC or shXPO6 #1 and 3, and subjected to colony formation assays. Western blot was performed to confirm XPO6 knockdown efficiency with tubulin as the loading control. Colony areas were quantified by ImageJ, and relative effects of XPO6 knockdown were expressed as fold changes in colony areas of shXPO6-infected cells over those infected with shLUC. Data are mean ± SD of one representative experiment (quadruplicates per condition). P values were based on unpaired t-test by comparing shXPO6 infected cells to those with shLUC. Results were confirmed three times independently. (C) Western blot analysis showing overexpression of XPO6 lacking (WT) or containing silent mutations (RNAi-Res) in MCF-7 cells by lentiviral infection. Vector-infected cells show endogenous level of XPO6. GAPDH was blotted as the loading control. **, P<0.01, ****; P<0.0001.

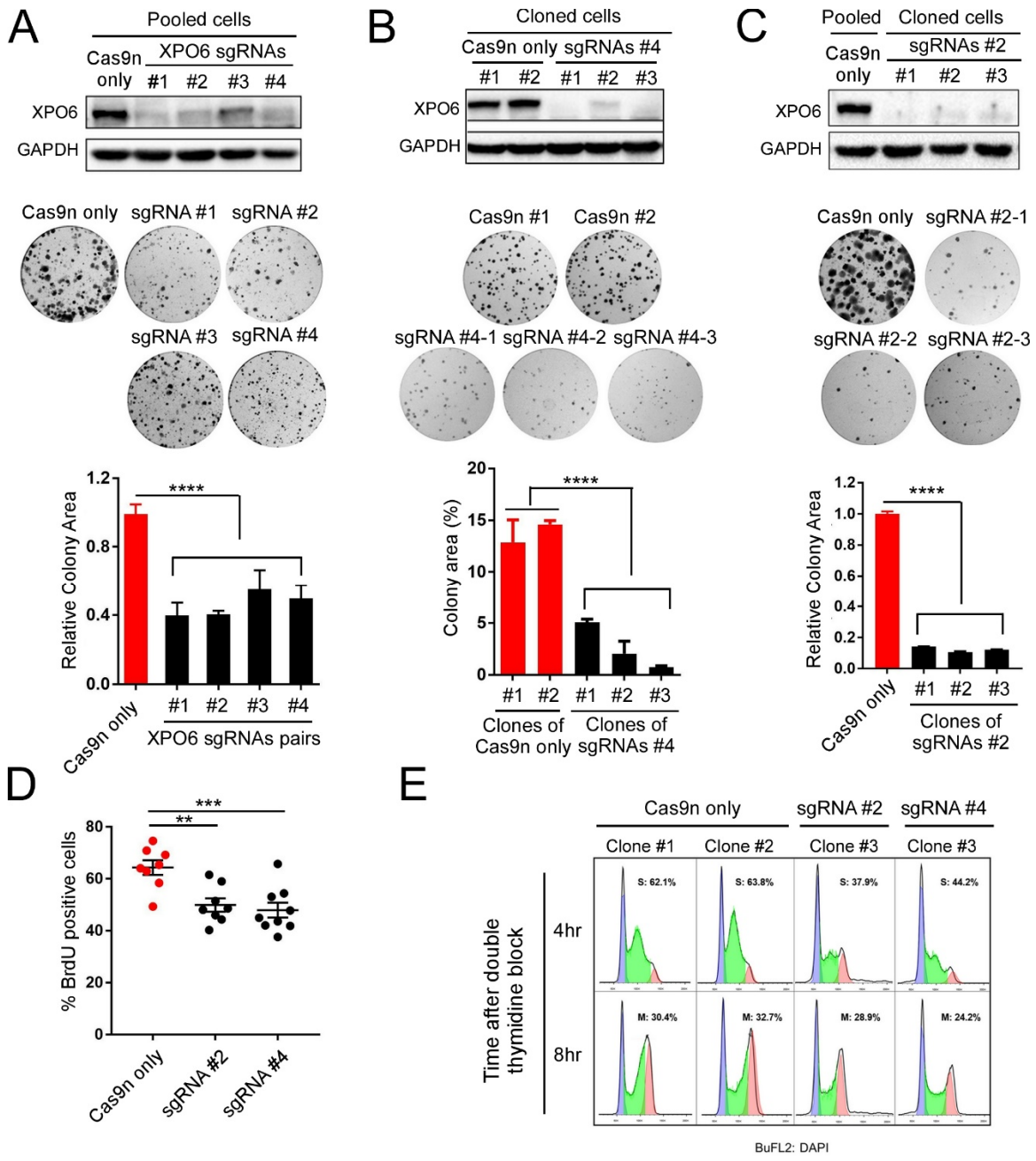


**Fig. S4 Effect of *XPO6* knockout by CRISPR/Cas9 on MDA-MB-231 cell cycle progression and growth *in vitro*, related to Figure 2.**

(A) MDA-MB-231 cells were transiently transfected with Cas9n alone or together with four pairs of gRNAs targeting different regions of human *XPO6*. Cells were selected with puromycin for three days, expanded in its absence, and analyzed by Western blot for XPO6 and GAPDH. They were subsequently compared for colony formation abilities. (B) Single clones selected from Cas9n or Cas9n/gRNAs #4-transfected MDA-MB-231 cells were subjected to Western blot analysis and colony formation assays. (C) Single clones selected from Cas9n/gRNAs #2-transfected MDA-MB-231 cells were subjected to Western blot analysis and colony formation assays as compared to pooled Cas9n only control cells. For A-C, data are mean ± SD of a representative experiment (triplicates per condition). P values for A and C were based on one-way ANOVA with Dunnett's multiple comparison tests. P values for B were based on one-way ANOVA with Tukey's multiple comparison tests. Results were confirmed three times independently. (D) Pooled MDA-MB-231 cells from (A) were pulsed and stained for BrdU. Total cells were stained by propidium iodide. Percentages of BrdU-positive cells and p values were calculated as in Fig.2F. (E) Clones of MDA-MB-231 cells transfected with

Cas9n or Cas9n/gRNA #2 and #4 as in (B-C) were subjected to DNA content analysis after double thymidine block and release, as described in 2G. For all the statistical analyses, **, p<0.01; ***, p<0.001; ****, p<0.0001.

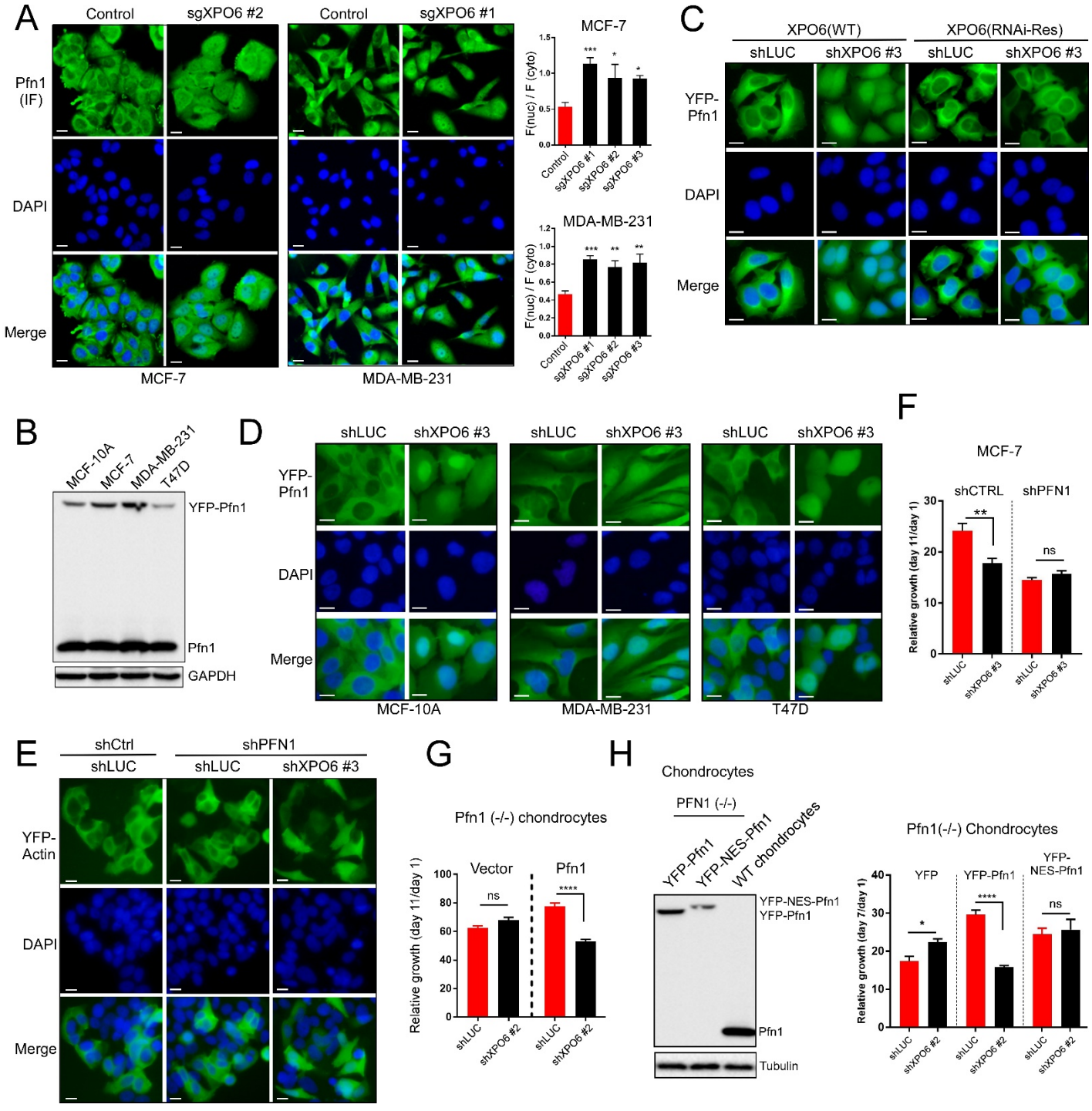


**Fig.S5 Effect of XPO6 loss on subcellular localization of Pfn1 and actin in breast epithelial cell lines, related to Figure.4.**

(A) MCF-7 and MDA-MB-231 cells were infected with control or sgXPO6-expressing lentiviruses and subjected to immunofluorescence staining for endogenous Pfn1 and nuclear counterstaining with DAPI. Representative images were shown to the left. More than >1000 cells per condition were analyzed by ImageJ to quantitatively compare relative Pfn1 intensity in the nucleus vs. cytoplasm (ratio). One-way ANOVA and Dunnett's multiple comparison tests (sgXPO6 vs. control) were used to calculate p values. Scale bars, 20μm.

(B) Western blot showing relative expression level of exogenous YFP-Pfn1 compared to endogenous Pfn1 in various cell lines. (C) MCF-7 cells expressing YFP-Pfn1 and XPO6 (WT) or XPO6 (RNAi-resistant) were infected with shLUC or shXPO6 #3, and analyzed by direct fluorescence after fixation and DAPI staining. Scale bars, 20µm. (D) YFP-Pfn1-expressing MCF-10A, MDA-MB-231, and T47D cells were infected with shLUC or shXPO6 (#3) and imaged for YFP-Pfn1 and DAPI as described in C. Scale bars, 20µm. (E) MCF-7 cells were sequentially infected with shLUC or shXPO6 (#3) and shCTRL or shPFN1 (#2), followed by transient transfection with YFP-actin. YFP-actin-positive cells were imaged by direct fluorescence after fixation and DAPI staining. Effects of XPO6 loss on YFP-Pfn1 and YFP-actin subcellular localization in C-E were confirmed by more than three independent experiments, each consisting of >100 cells. Scale bars 20µm. (F) MCF-7 cell growth rates in 2D culture (Day 11/Day 1 ratio) after single or double knockdown of XPO6 and Pfn1, related to Fig.4B. (G) Growth rates of *Pfn1*-null mouse chondrocytes re-infected with empty vector or untagged Pfn1 in 2D culture (ratio Day 11/Day 1), related to Fig.4C. (H) *Pfn1*-null mouse chondrocytes were re-infected with YFP, YFP-Pfn1(WT), or YFP-NES-Pfn1(WT), and subjected to Western blot and 2D growth assay as described in F-G, related to Fig.4D. Expression levels of transduced Pfn1 fusion proteins were compared to endogenous Pfn1 in wild type mouse chondrocytes. Data in F-H are mean ± SEM of a representative experiment (sextuplicates per condition). P values in F-H were based on one-way ANOVA and Tukey's multiple comparison tests. Results were confirmed by three independent experiments. For all the statistical analyses, *, p<0.05; **, p<0.01; ***, p<0.001; ****, p<0.0001.

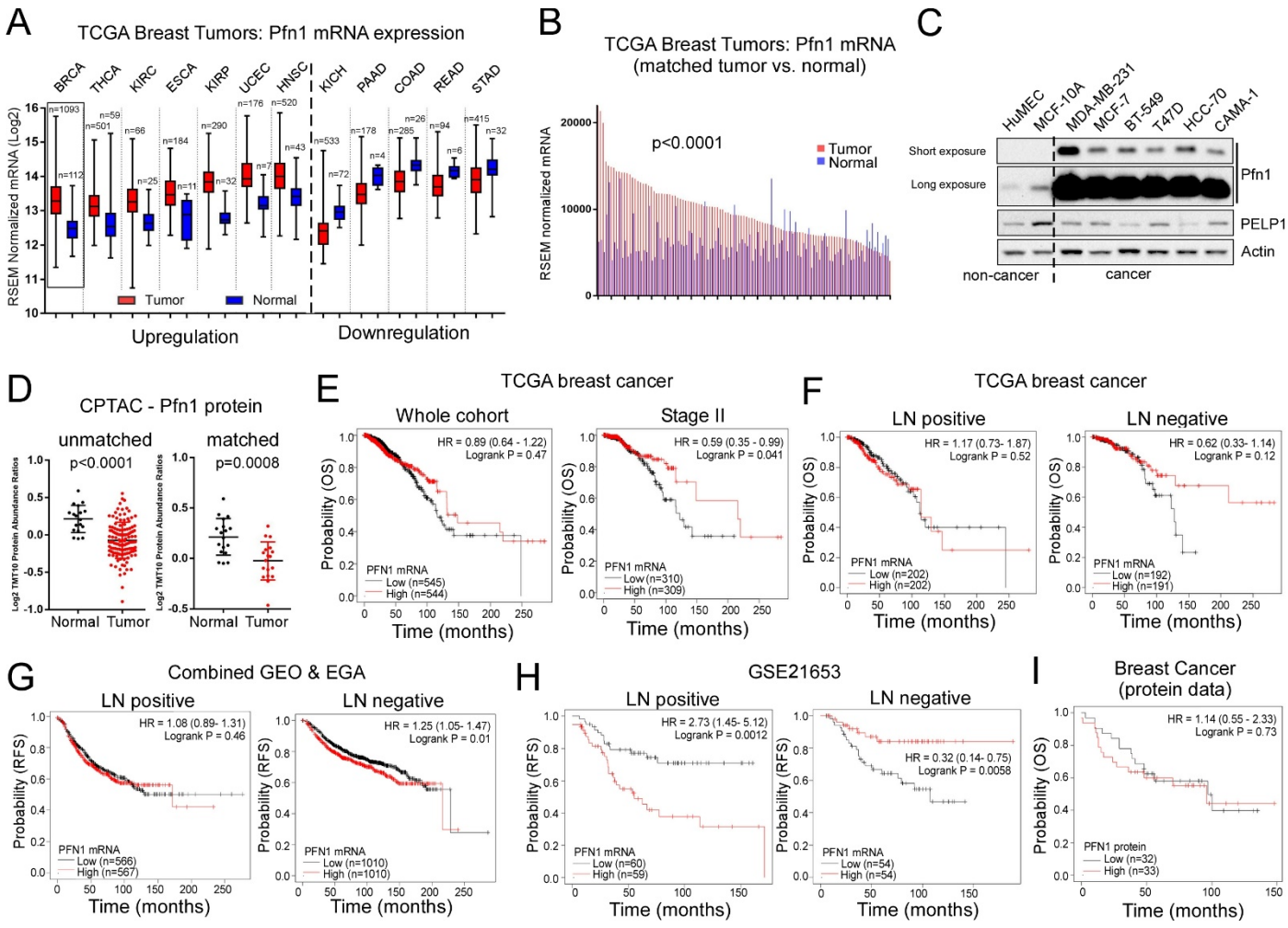


**Fig. S6 *Pfn1* mRNA and protein level in breast cancer, related to Figure 4.**
(A) TCGA cohorts in which *Pfn1* mRNA level is significantly altered relative to normal tissues. Whiskers represent min-max. Mann-Whitney U non-parametric test was used to calculate statistical significance (values in Table S1D). (B) *Pfn1* mRNA levels of 112 TCGA breast tumors compared with their adjacent normal tissues.

P value is based on Wilcoxon Signed Rank non-parametric test. (C) Western blot analysis for Pfn1 in untransformed and transformed breast epithelial cell lines (same panel as in Fig.1D). Actin and PELP1 were used as cytoplasmic and nuclear control proteins. (D) Pfn1 protein level in the CPTAC confirmatory breast tumor cohort detected by quantitative mass spectrometry analysis. Unpaired comparison between the 125 breast tumors and 18 normal tissues was shown to the left. Paired comparison of the 18 breast tumors with their adjacent normal tissues was shown to the right. P values were based on Mann-Whitney U non-parametric test (unpaired comparison) and Wilcoxon Signed Rank non-parametric test (paired comparison). (E) Univariate Kaplan-Meier analysis of the association between *Pfn1* mRNA level and the overall survival (OS) of breast cancer patients in the TCGA dataset. Analysis was performed by KM plotter for the entire cohort or stage II patients. (F) Univariate Kaplan-Meier analysis of the association between *Pfn1* mRNA level and the overall survival (OS) of breast cancer patients in the TCGA dataset divided based on lymph node status. (G) Univariate Kaplan-Meier analysis of the association between *Pfn1* mRNA level and the overall survival (RFS) of breast cancer patients in the combined GEO and EGA datasets divided by lymph node. (H) Univariate Kaplan-Meier analysis of the association between *Pfn1* mRNA level and the overall survival (RFS) of breast cancer patients in the GSE21653 dataset divided by lymph node status. (I) Univariate Kaplan-Meier analysis of the association between Pfn1 protein level and the overall survival (OS) of a cohort of 65 breast cancer patients using KM plotter. For (E-I), median cutoff was used for patient separation. P values were based on log-rank test.

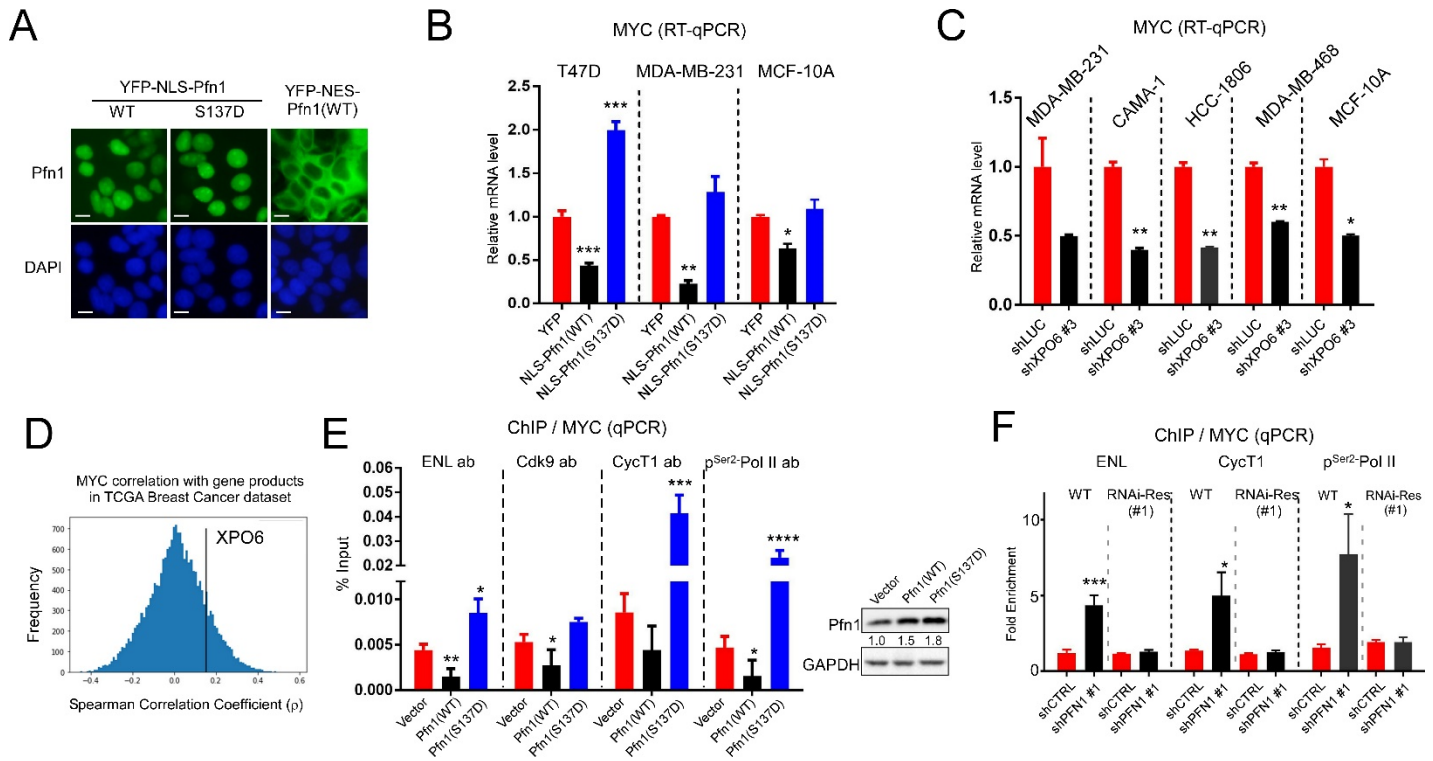


**Fig.S7 Inhibition of SEC function by nuclear Pfn1, related to Figure 6.**
(A) Direct fluorescence imaging of MCF-7 cells expressing YFP-tagged NLS-Pfn1(WT or S137D) or NES-Pfn1(WT). Scale bars, 20μm. (B) RT-qPCR analysis of *MYC* expression level in different breast epithelial cell lines expressing YFP, YFP-NLS-Pfn1(WT), or YFP-NLS-Pfn1(S137D). P values were based on unpaired t-test by comparing NLS-Pfn1(WT or S137D) vs. YFP. (C) RT-qPCR analysis of *MYC* expression level in different breast epithelial cell lines infected with shLUC or shXPO6 #3. P values were based on unpaired t-test by comparing shLUC vs. shXPO6. (D) Distribution of all genes in the TCGA breast cancer dataset based on the correlation of their mRNA levels with that of *MYC*. Spearman correlation coefficient was used (ρ, x-axis). Y-axis reflects the number of genes correlating with *MYC* with a given ρ value. (E) Chromatin IP using antibodies against SEC components (ENL, Cyclin T1, Cdk9) and pSer$^2$-Rpb1 from MCF-7 cells infected with vector only or untagged Pfn1(WT) or Pfn1(S137D), followed by qPCR using *MYC* primers as in Fig.6H and 6I. Percentages of input were used for quantification. P values were based on unpaired t-test by comparing Pfn1(WT or S137D)

vs. vector. Western blot and densitometry show the relative expression level of exogenous Pfn1 to endogenous Pfn1. (F) Chromatin IP using antibodies against ENL, Cyclin T1, and pSer$^{2}$-Rpb1 from MCF-7 cells stably expressing Pfn1(WT) or Pfn1(RNAi-Res) and infected with shCTRL or shPFN1 (#1), followed by qPCR using *MYC* primers as in (B). Fold enrichment of each target protein over control IgG was used for quantification. P values were based on unpaired t-test by comparing shPFN1 vs. shCTRL within Pfn1(WT) or Pfn1(RNAi-Res) cells. For all the statistical analyses, *, p<0.05; **, p<0.01; ***, p<0.001; ****, p<0.0001.

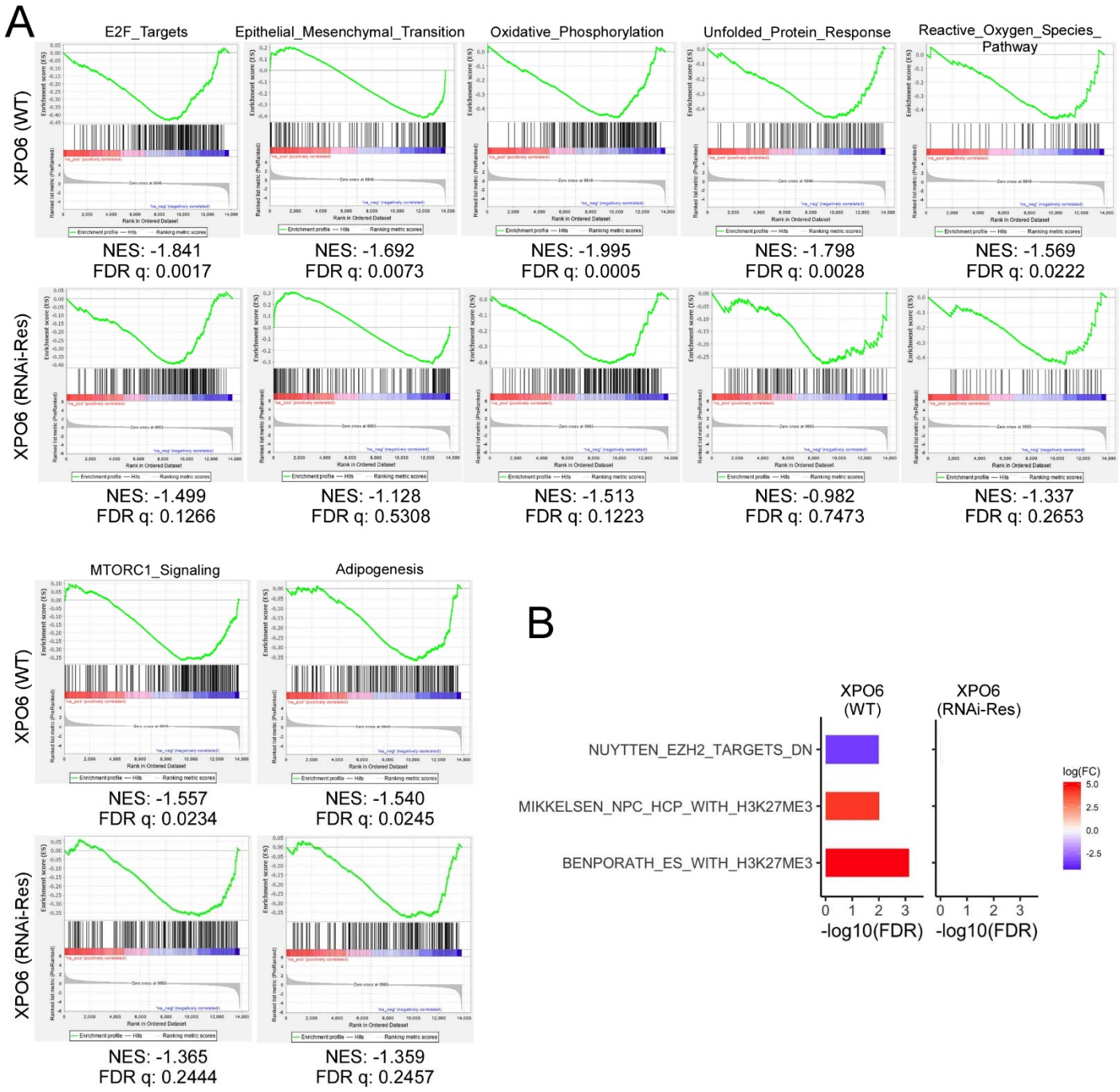


**Fig.S8 Transcriptomic effects of XPO6 loss, related to Fig.7.**
(A) Gene set enrichment analysis (GSEA) evaluating shXPO6-induced gene expression changes in MCF-7 cells expressing XPO6(WT) or XPO6(RNAi-R) using the MSigDB hallmark (50 gene sets) database. Shown are seven significantly enriched hallmark gene sets in addition to the two gene sets shown in Fig.7A (related to Table S4A). FDR, false discovery rate; NES, normalized enrichment score. (B) Representative gene sets (EZH2 repressed targets bearing H3K27me3) in the curated MSigDB chemical and genetic perturbations (CGP) gene

sets (3302 gene sets) which are significantly enriched in shXPO6-infected XPO6(WT)-expressing MCF-7 cells, using GAGE analysis. Changes in the XPO6(RNAi-Res)-expressing MCF-7 cells are shown as the control.

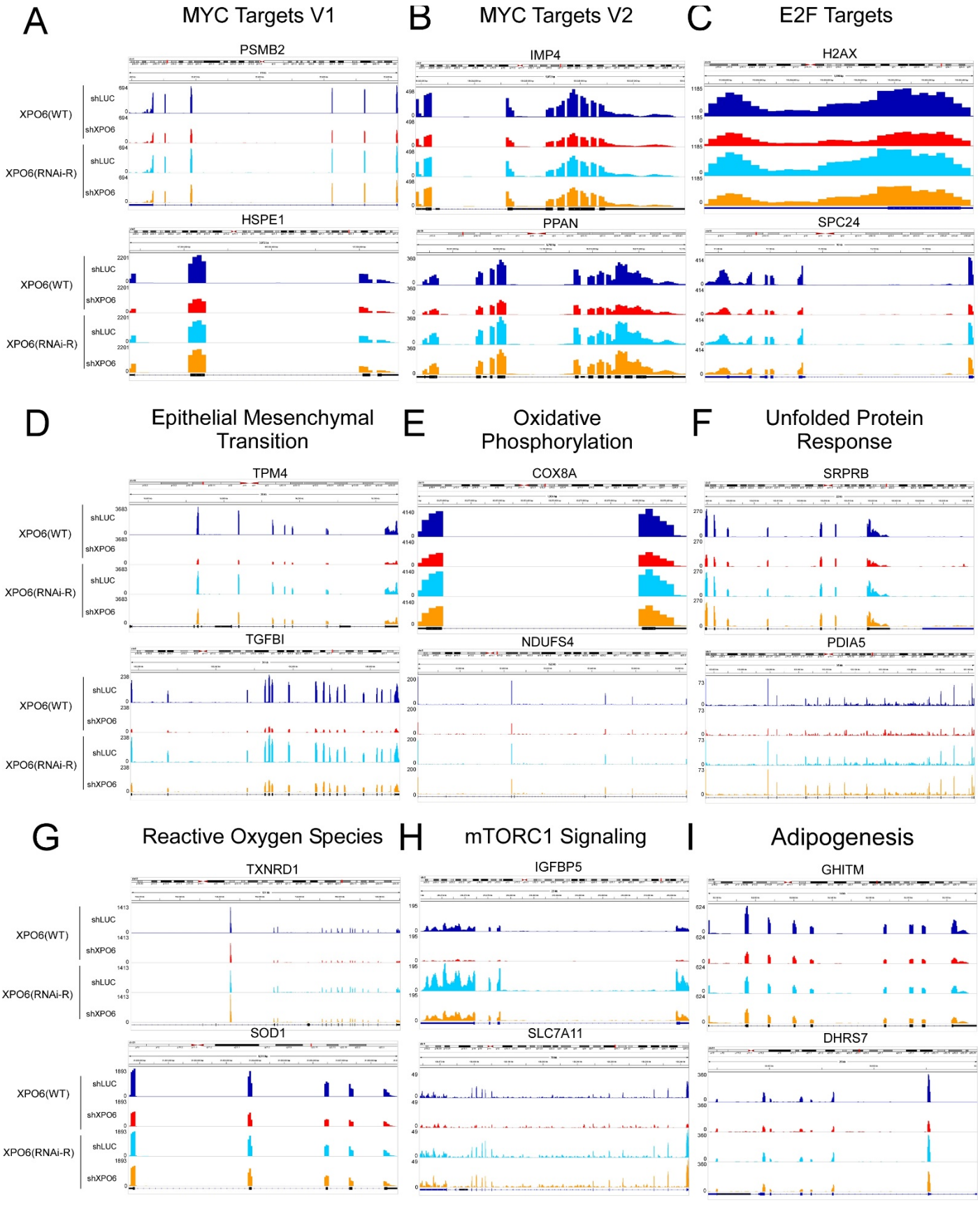

**Fig.S9 RNA-seq tracks of representative genes in the significantly enriched hallmark gene sets by XPO6 knockdown based GSEA analysis, related to Fig.7 and Fig.S8A.** Two representative genes are selected from each of the nine hallmark gene sets significantly enriched by XPO6 knockdown in MCF-7 cells based on gene set enrichment analysis (GSEA). RNA-seq reads are shown for all four experimental conditions including XPO6(WT) and XPO6(RNAi-R) cells infected with shLUC or shXPO6. Each track represents the sum of RPKM-normalized reads (Y-axis) from two replicate RNA-seq experiments.

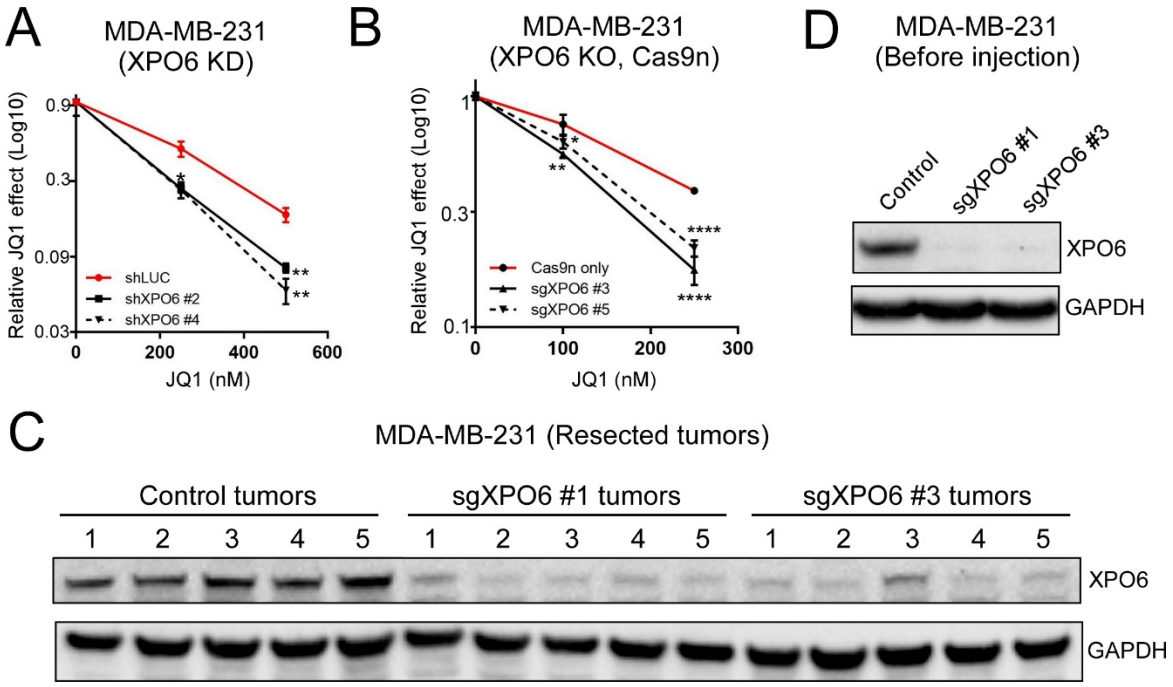


**Fig.S10 *In vitro* JQ1-sensitizing effect of XPO6 loss, related to Fig.7.**
(A) MDA-MB-231 cells infected with shLUC or two different shXPO6 viruses were treated with DMSO or JQ1 at different concentrations in colony formation assays for 8 days, and quantified by Alamar blue. Relative drug effect was calculated by dividing JQ1-treated cell numbers by those treated with vehicle. P values were based on one-way ANOVA and Dunnett's multiple comparisons by comparing sXPO6 and shLUC at different JQ1 concentrations. (B) MDA-MB-231 cells transfected with Cas9n or Cas9n with two pairs of XPO6-specific gRNAs were treated with DMSO or JQ1 for 7 days in colony formation assays and quantified by Alamar blue. Relative drug effects and p values were calculated as in (A). (C) Western blot showing high *XPO6* KO efficiency in the MDA-MB-231 cells before inoculation in mice. (D) Western blot showing largely sustained *XPO6* KO efficiency in the resected tumors. Five tumors from the vehicle groups of control and sgXPO6 mice were randomly chosen. For all the statistical analyses, *, $p<0.05$; **, $p<0.01$; ****, $p<0.0001$.

**Supplementary Tables**

**Table S2 List of nuclear proteins specifically detected by co-immunoprecipitation and LC-MS to interact with NLS-Pfn1(WT), related to Fig.5B.**

| LFQ Intensity | | | LFQ ratio Pfn1(WT) vs. Pfn1(S137D) | LFQ ratio Pfn1(WT) vs. YFP | Protein ID (HUGO names) | PLP motifs ($XP_n$, n≥5; X=A, I, L, S, G) |
|---|---|---|---|---|---|---|
| YFP | Pfn1 (WT) | Pfn1 (S137D) | | | | |
| 0 | 5669.3 | 0 | N/A | N/A | HIST1H1C;HIST1H1E; HIST1H1D | |
| 0 | 3193.4 | 0 | N/A | N/A | SERBP1 | |

| | | | | | | |
|---|---|---|---|---|---|---|
| 0 | 2765.7 | 0 | N/A | N/A | ZMYM4 | |
| 0 | 2516.6 | 0 | N/A | N/A | **SFPQ** | **IP5, QP5, GP5** |
| 0 | 2323 | 0 | N/A | N/A | NCL | |
| 0 | 2243.7 | 0 | N/A | N/A | U2AF1;U2AF1L4 | |
| 0 | 1906.9 | 0 | N/A | N/A | PDLIM5 | |
| 0 | 1344.4 | 0 | N/A | N/A | RPL28 | |
| 0 | 1190.8 | 0 | N/A | N/A | *SEPTIN9* | |
| 0 | 1149.3 | 0 | N/A | N/A | YBX1 | |
| 0 | 1148.9 | 0 | N/A | N/A | HP1BP3 | |
| 0 | 1089.1 | 0 | N/A | N/A | EEF1G | |
| 0 | 1070.6 | 0 | N/A | N/A | AFF4 | |
| 0 | 1035.4 | 0 | N/A | N/A | OARD1 | |
| 0 | 963.61 | 0 | N/A | N/A | NACC1 | |
| 0 | 755.65 | 0 | N/A | N/A | ACYP2 | |
| 0 | 678.92 | 0 | N/A | N/A | SDHA | |
| 0 | 653.04 | 0 | N/A | N/A | SPTBN1 | |
| 0 | 653.03 | 0 | N/A | N/A | ELL | |
| 0 | 648.88 | 0 | N/A | N/A | NBN | |
| 0 | 561.46 | 0 | N/A | N/A | THOC1 | |
| 0 | 556.13 | 0 | N/A | N/A | TPR | |
| 0 | 495.84 | 0 | N/A | N/A | NPM1 | |
| 0 | 436.67 | 0 | N/A | N/A | TP53BP1 | |
| 0 | 426.69 | 0 | N/A | N/A | TRIP6 | |
| 0 | 383.43 | 0 | N/A | N/A | **BOD1L1** | **AP6, QP6** |
| 0 | 376.2 | 0 | N/A | N/A | USP48 | |
| 0 | 299.3 | 0 | N/A | N/A | SEC24B | |
| 0 | 291.88 | 0 | N/A | N/A | CAMK2D;CAMK2G; CAMK2B;CAMK2A | |
| 0 | 280.5 | 0 | N/A | N/A | RTCB | |
| 0 | 278.72 | 0 | N/A | N/A | DOCK1 | |
| 520.9 | 1429.1 | 0 | N/A | 2.743521 | SLC9A3R2 | |
| 0 | 574.58 | 128.49 | 4.471788 | N/A | **MLLT1 (ENL)** | **GP9** |
| 1182.2 | 4379 | 1546.4 | 2.831738 | 3.704111 | NONO | |
| 0 | 4116.9 | 1649.9 | 2.495242 | N/A | TOP1 | |
| 0 | 2032.4 | 900.98 | 2.255766 | N/A | CCNT1 (Cyclin T1) | |
| 4440.4 | 9207.2 | 5605.6 | 1.6425 | 2.073507 | MYH9 | |
| 0 | 9049.7 | 12121 | 0.746613 | N/A | PFN1 (Profilin-1) | |

**Table S3 Correlation analysis of *MYC* mRNA level in TCGA datasets with those of *XPO6, BRD4*, and *NCL*, related to Fig.6G.**

| Cancer type | Case number | Gene correlated with MYC | Correlation coefficient (ρ) | FDR q-values |
|---|---|---|---|---|
| **Positive correlation between XPO6 and MYC, statistically significant** | | | | |
| BLCA | 408 | XPO6 | 0.352872 | 0.0000 |
| BLCA | 408 | BRD4 | 0.112877 | 0.0444 |

| | | | | |
|---|---|---|---|---|
| BLCA | 408 | NCL | 0.510321 | 0.0000 |
| BRCA | 1093 | XPO6 | 0.152878 | 0.0000 |
| BRCA | 1093 | BRD4 | 0.232964 | 0.0000 |
| BRCA | 1093 | NCL | 0.329715 | 0.0000 |
| CESC | 304 | XPO6 | 0.307644 | 0.0000 |
| CESC | 304 | BRD4 | 0.235313 | 0.0001 |
| CESC | 304 | NCL | 0.260244 | 0.0000 |
| COAD | 285 | XPO6 | 0.254252 | 0.0001 |
| COAD | 285 | BRD4 | 0.139062 | 0.0382 |
| COAD | 285 | NCL | 0.380718 | 0.0000 |
| ESCA | 184 | XPO6 | 0.29624 | 0.0001 |
| ESCA | 184 | BRD4 | 0.305099 | 0.0001 |
| ESCA | 184 | NCL | 0.268953 | 0.0006 |
| GBM | 153 | XPO6 | 0.227795 | 0.0107 |
| GBM | 153 | BRD4 | 0.405643 | 0.0000 |
| GBM | 153 | NCL | 0.215412 | 0.0167 |
| HNSC | 520 | XPO6 | 0.288748 | 0.0000 |
| HNSC | 520 | BRD4 | 0.129335 | 0.0078 |
| HNSC | 520 | NCL | 0.346166 | 0.0000 |
| KIRP | 290 | XPO6 | 0.386741 | 0.0000 |
| KIRP | 290 | BRD4 | 0.114534 | 0.0893 |
| KIRP | 290 | NCL | 0.318328 | 0.0000 |
| LGG | 516 | XPO6 | 0.337445 | 0.0000 |
| LGG | 516 | BRD4 | 0.218876 | 0.0000 |
| LGG | 516 | NCL | 0.363515 | 0.0000 |
| LUAD | 515 | XPO6 | 0.10036 | 0.0444 |
| LUAD | 515 | BRD4 | 0.102506 | 0.0400 |
| LUAD | 515 | NCL | 0.279344 | 0.0000 |
| LUSC | 501 | XPO6 | 0.208782 | 0.0000 |
| LUSC | 501 | BRD4 | 0.284897 | 0.0000 |
| LUSC | 501 | NCL | 0.252379 | 0.0000 |
| PAAD | 178 | XPO6 | 0.242768 | 0.0029 |
| PAAD | 178 | BRD4 | 0.129126 | 0.1387 |
| PAAD | 178 | NCL | 0.349089 | 0.0000 |
| SARC | 259 | XPO6 | 0.181895 | 0.0079 |
| SARC | 259 | BRD4 | -0.00447 | 0.9464 |
| SARC | 259 | NCL | 0.295661 | 0.0000 |
| STAD | 415 | XPO6 | 0.222563 | 0.0000 |
| STAD | 415 | BRD4 | 0.027652 | 0.6611 |
| STAD | 415 | NCL | 0.372324 | 0.0000 |
| THYM | 120 | XPO6 | 0.461317 | 0.0000 |
| THYM | 120 | BRD4 | 0.098028 | 0.3731 |
| THYM | 120 | NCL | 0.421488 | 0.0000 |
| **Positive correlation between XPO6 and MYC, statistically insignificant** | | | | |
| OV | 303 | XPO6 | 0.078555 | 0.2452 |
| OV | 303 | BRD4 | 0.007782 | 0.9275 |
| OV | 303 | NCL | 0.19199 | 0.0021 |

| | | | | |
|---|---|---|---|---|
| SKCM | 103 | XPO6 | 0.155285 | 0.1822 |
| SKCM | 103 | BRD4 | 0.184719 | 0.1043 |
| SKCM | 103 | NCL | 0.216481 | 0.0522 |
| UCEC | 176 | XPO6 | 0.10687 | 0.2286 |
| UCEC | 176 | BRD4 | 0.334733 | 0.0000 |
| UCEC | 176 | NCL | 0.504854 | 0.0000 |
| UCS | 57 | XPO6 | 0.154784 | 0.3310 |
| UCS | 57 | BRD4 | 0.355847 | 0.0149 |
| UCS | 57 | NCL | 0.225694 | 0.1434 |
| PRAD | 497 | XPO6 | 0.082714 | 0.1079 |
| PRAD | 497 | BRD4 | 0.128944 | 0.0094 |
| PRAD | 497 | NCL | 0.381517 | 0.0000 |
| ACC | 79 | XPO6 | 0.129747 | 0.3337 |
| ACC | 79 | BRD4 | 0.070058 | 0.6301 |
| ACC | 79 | NCL | 0.482157 | 0.0000 |
| CHOL | 36 | XPO6 | 0.166281 | 0.4188 |
| CHOL | 36 | BRD4 | 0.02677 | 0.9190 |
| CHOL | 36 | NCL | 0.63861 | 0.0001 |
| DLBC | 48 | XPO6 | 0.070126 | 0.7064 |
| DLBC | 48 | BRD4 | 0.277681 | 0.0964 |
| DLBC | 48 | NCL | 0.67271 | 0.0000 |
| KICH | 66 | XPO6 | 0.012671 | 0.9428 |
| KICH | 66 | BRD4 | 0.16969 | 0.2452 |
| KICH | 66 | NCL | 0.0401 | 0.8155 |
| LIHC | 371 | XPO6 | 0.016098 | 0.8187 |
| LIHC | 371 | BRD4 | -0.08045 | 0.1852 |
| LIHC | 371 | NCL | 0.519352 | 0.0000 |
| OV | 303 | XPO6 | 0.078555 | 0.2452 |
| OV | 303 | BRD4 | 0.007782 | 0.9275 |
| OV | 303 | NCL | 0.19199 | 0.0021 |

P-values calculated from the Spearman correlation were subjected to multiple hypothesis correction using the Benjamini-Hochberg method to generate FDR q-values.